

RICE UNIVERSITY

**Intersubband Transitions
in Narrow InAs/AlSb Quantum Wells**

by

Diane Larrabee

A THESIS SUBMITTED
IN PARTIAL FULFILLMENT OF THE
REQUIREMENTS FOR THE DEGREE

Master of Science

APPROVED, THESIS COMMITTEE:

Junichiro Kono, Assistant Professor, Chair
Electrical and Computer Engineering

Frank K. Tittel, J. S. Abercrombie Professor
Electrical and Computer Engineering

Naomi J. Halas, Stanley C. Moore Professor
Electrical and Computer Engineering
and Professor, Chemistry

HOUSTON, TEXAS

OCTOBER 2003

Abstract

Intersubband resonances in InAs/AlSb are an ideal tool for optically pumped terahertz (THz) generation because of their enormous tunability and their strength at room temperature. We have carried out a systematic temperature-dependent study of intersubband absorption in InAs/AlSb quantum wells from 5 to 10 nm well width. The resonance energy redshifts with increasing temperature from 10 to 300 K, and the amount of redshift increases with decreasing well width. We have also observed intersubband absorption in wells as narrow as 3 nm, investigated the carrier distribution in the wells and its influence on the intersubband absorption, and performed temperature-dependent cyclotron resonance using a THz quantum cascade laser. We have observed multiple intersubband resonances in coupled quantum well structures designed for THz difference frequency generation. We have modeled the resonances using eight-band $\mathbf{k}\cdot\mathbf{p}$ theory combined with semiconductor Bloch equations, including the main many-body effects. Temperature is incorporated via band filling and nonparabolicity, and good agreement with experiment is achieved for the temperature dependence of the resonance.

Acknowledgements

This thesis describes a collaboration between three groups. The samples were grown at Osaka Institute of Technology in Osaka, Japan, by K. Ueda, Y. Nakajima, M. Nakai, S. Suekane, and Profs. S. Sasa and M. Inoue. In addition to growth, this group characterized the samples by X-ray diffraction, photoluminescence, Hall measurements, and Shubnikov-de Haas (SdH) measurements. The intersubband absorption measurements were done at Rice University by the author. J. Tang made some absorption measurements and made the TEM samples, B. E. Brinson made the TEM measurements, M. Liang did absorption sample preparation, S. M. Crankshaw built the SdH sample holder and made SdH measurements, G. G. Walden helped with the absorption measurements and cyclotron resonance, and Dr. G. A. Khodaparast did the Landau level calculations for cyclotron resonance. Dr. F. K. Tittel borrowed the THz quantum cascade lasers (QCLs) from their developer, Dr. J. Faist of the University of Neuchatel, Switzerland. Dr. G. A. Khodaparast provided essential guidance and expertise throughout these efforts. Prof. J. Kono leads the entire project. The $\mathbf{k}\cdot\mathbf{p}$ calculations and absorption modeling were done at NASA Ames Research Center, Moffett Field, California, by Dr. K. I. Kolokolov, Dr. J. Li, and Dr. C. Z. Ning. We gratefully acknowledge support from DARPA/AFOSR F49620-01-1-0543 (ABCS), NASA-NCIBSRP, the Robert A. Welch Foundation, NSF DMR-0134058 (CAREER), and NSF INT-0221704.

I would like to thank the many people at Rice who have helped me, including: Michael Dye, all of Alex Rimberg's group, past and present, who maintain their evaporator and let me use it, Adrian Barkan, Yuri Bakhirkin, and Anatoliy Kosterev, who

helped me figure out how to use the QCLs, and Dr. Kono's group. I would like to thank my advisor, Dr. Kono, whose extensive understanding of the interaction of light with semiconductors enables him to guide this project in interesting and fruitful directions. I would especially like to thank Giti Khodaparast, who besides patiently teaching me many laboratory techniques and approaches has also demonstrated how to rent a sedan when offered a pick-up. Finally, I would like to thank my family and friends for all of their support.

CONTENTS

1	MOTIVATION	7
1.1	THE THZ GAP	7
1.2	WHY INAS/ALSB?	9
2	SAMPLE GROWTH AND CHARACTERIZATION.....	12
2.1	SAMPLE STRUCTURE	12
2.2	TRANSPORT MEASUREMENTS	14
2.2.1	<i>Theory</i>	14
2.2.2	<i>Temperature-dependent Hall measurements</i>	19
2.2.3	<i>Carrier distribution</i>	20
2.3	CYCLOTRON RESONANCE	21
2.4	TEM	25
2.5	PHOTOLUMINESCENCE	25
3	INTERSUBBAND ABSORPTION.....	27
3.1	SELECTION RULES AND EXPERIMENTAL GEOMETRY	27
3.2	INTERBAND ABSORPTION	30
3.3	TEMPERATURE DEPENDENCE OF ISBAS IN MEDIUM-DENSITY WELLS.....	31
3.4	ELECTRON DENSITY AND DISTRIBUTION—COMPARISON OF 10 NM QWS	32
3.4.1	<i>Low vs. high density</i>	33
3.4.2	<i>Single vs. multiple wells</i>	34
3.4.3	<i>InAs vs. GaSb cap</i>	35
3.4.4	<i>Thick vs. thin ALSb top barrier</i>	35
3.5	DOPING	36
3.6	HIGH ENERGY ISBA.....	37
3.7	UN-LIKE INTERFACES	38
3.8	COUPLED DOUBLE QUANTUM WELLS.....	40
3.8.1	<i>Symmetric</i>	40
3.8.2	<i>Asymmetric</i>	41
3.9	EXPERIMENTAL CONUNDRUMS.....	43
3.9.1	<i>GaSb substrate</i>	43
3.9.2	<i>Wiggles</i>	44
3.9.3	<i>Unexpectedly large absorption</i>	45
3.9.4	<i>Non-zero baseline</i>	45
3.10	SUMMARY	46
4	THEORETICAL MODELING	47
4.1	K·P MODEL.....	47
4.1.1	<i>Bulk dispersion relations</i>	47
4.1.2	<i>Heterostructure: Envelope Function description</i>	52
4.2	ABSORPTION CALCULATION.....	55
4.2.1	<i>Intersubband Semiconductor Bloch Equations</i>	55
4.2.2	<i>Many-body Effects</i>	57
4.2.3	<i>Temperature dependence</i>	59
5	CONCLUSIONS	60
6	APPENDIX A: HOW-TO	61
6.1	ANNEALING IN CONTACTS FOR TRANSPORT MEASUREMENTS.....	61
6.1.1	<i>How to make your own annealing box</i>	63
6.2	ELECTRICAL SET-UP FOR SDH/HALL MEASUREMENTS	63
6.3	GOLD COATING FOR ISBA MEASUREMENTS.....	63

6.4	POLISHING FOR ISBA MEASUREMENTS.....	64
7	APPENDIX B: SAMPLES	66
8	REFERENCES.....	75

1 Motivation

1.1 The THz gap

The terahertz (THz) region of the electromagnetic spectrum, from 1 to 10×10^{12} Hz (300-30 μm ; 4-40 meV), is rich with possibilities for communications, chemical sensing, astronomy, and condensed matter spectroscopy.^{1,2} But, this spectral range is currently under-utilized due to a lack of convenient sources and detectors. Approaching the THz from the high-energy side, optical sources are limited by the difficulty of creating materials with a small enough energy level separation. Thermal population of those levels is also an obstacle, since $k_B \times 300 \text{ K} = 26 \text{ meV} = 6 \text{ THz}$.

A variety of coherent THz sources exist. Molecular gas lasers have many lines in the far-infrared. Broadly tunable or broadband THz sources include the free electron laser,³ *p*-type germanium laser,⁴ and Auston switches.⁵ These sources are cumbersome, however, requiring significant infrastructure or cryogenic cooling. Compact, table-top sources include optical rectification of fs pulses at semiconductor surfaces⁶ and in periodically poled lithium niobate,^{7,8} photomixing of visible diode lasers in low temperature grown GaAs,⁹ and THz optical parametric oscillators.¹⁰

One remarkable new single-color THz source is the quantum cascade laser (QCL). First demonstrated in the midinfrared,¹¹ this unipolar, electrically driven laser is based on transitions between quantized levels in narrow quantum well structures (Fig. 1). Design improvements have led to lasing at wavelengths as long as 100 μm (3.0 THz) with peak powers (pulsed) as high as 1.5 mW at 4 K.^{12,13,14} Despite the remarkable achievements of

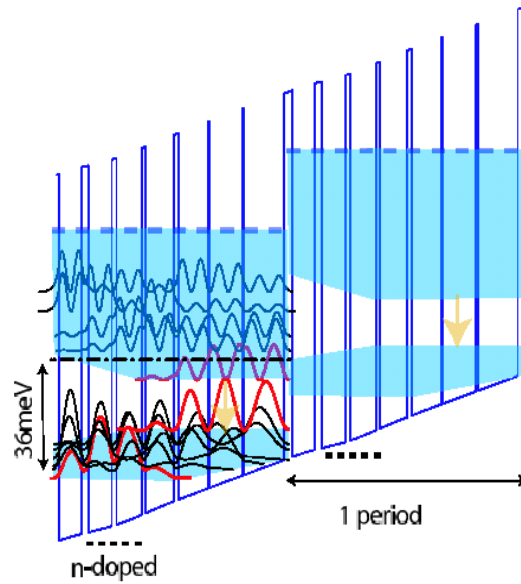


Figure 1: Conduction band profile of a quantum cascade laser.

THz QCLs, they are subject to intrinsic limitations including free carrier absorption, which is proportional to the square of the emission wavelength, and reduction of population inversion due to electron-electron scattering. Both of these limitations are more significant at higher carrier densities. Therefore, it is worthwhile to investigate optically driven THz sources. These have fewer free carriers because they do not require heavily doped contact layers and because it is possible to create carriers only in selected regions by a judicious choice of pumping wavelengths. Fewer heterostructure layers and fewer free carriers may lead to compact devices with superior THz performance.

Several optically pumped THz sources have been demonstrated. O. Gauthier-Lafaye *et al.* created a three-level laser within the conduction band of GaAs/Al_{0.35}Ga_{0.65}As asymmetric coupled double quantum wells.¹⁵ It is pumped by a CO₂ laser and emits at 15.5 μm with a peak power of 0.4 W. C. Sirtori *et al.* demonstrated difference frequency mixing of CO₂ lasers in GaAs/Al_{0.33}Ga_{0.67}As symmetric coupled

double quantum wells, achieving up to 0.7 nW emission at 60 μm .¹⁶ One significant improvement in the convenience of these sources would be solid-state pumping, for example by a near-infrared (NIR) diode laser. But this is not possible in GaAs/Al_xGa_{1-x}As quantum wells, in which the conduction band (CB) offset is only about 1 eV for $x = 1$.¹⁷ The maximum possible intra-well pumping energy is less than this value. So in order to use a NIR pump, we must use a material system with a larger CB offset.

1.2 Why InAs/AlSb?

We have chosen to work with the 6.1 Å semiconductors: InAs, GaSb, and AlSb. The conduction band offsets in this material system are enormous—as much as 2 eV between InAs and AlSb—allowing great flexibility in wavefunction engineering.

Our device, like the other optically pumped THz sources described above, will be based on intersubband resonances. These have several advantages: 1) Intersubband transitions have giant oscillator strengths. They are by far the strongest optical transitions that are known to occur in semiconductors. 2) The transition energies (or wavelengths) of intersubband transitions are much less material-dependent than interband transitions. They are tunable within the nearly the entire range given by the band offset, whereas the transition energy of an interband transition has to be near the band gap of the material chosen. 3) Intersubband absorption does not lose its oscillator strength at high temperatures; it is strong at room temperature, with about half as much amplitude and sharpness as at low temperature. 4) Intersubband resonances are not strongly affected by low mobility in the quantum well. This is an advantage particularly in 6.1 Å materials because there is no easy way to remotely dope InAs/AlSb quantum wells *n*-type, so they must be doped in the well.

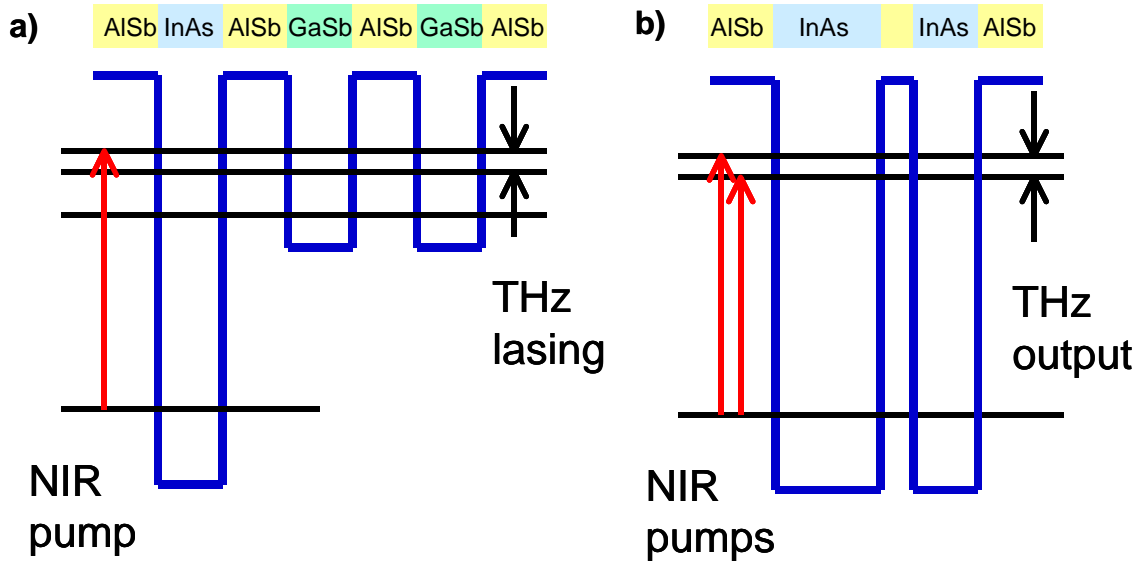


Figure 2: Conduction band profiles for (a) an antimonide based THz laser and (b) a THz difference frequency generator.

Figure 2(b) shows a cartoon of a difference frequency generation structure. The quantum wells are engineered to have intersubband resonance energies close to two pump energies. This creates a large second-order nonlinear optical susceptibility, which enables the production of light at the difference energy of the two pumps. Because of the large CB offset between InAs and AISb, it may be possible to create resonance energies in the near-infrared, where convenient diode laser pumps are available. Because the intersubband resonance is fairly robust with increasing temperature, it may be possible to use this structure at room temperature. Figure 2(a) shows a design for an intersubband THz laser.¹⁸ Because the intersubband pump energy is large, it is possible to locate the lasing levels well above the Fermi level and avoid thermal population of the lasing levels. One possible drawback of this design is interband absorption in the GaSb layers, if the pump photon energy exceeds its band gap (~ 0.8 eV).

In order to realize an intersubband optically pumped THz source, we must first thoroughly understand intersubband absorption (ISBA) in InAs/AISb QWs. We have

grown a variety of InAs/AlSb QWs in order to investigate the ISBA dependence on well width, temperature, carrier density and distribution, doping, and interface type. We have characterized the QWs by electrical transport, cyclotron resonance, and photoluminescence. We have observed ISBA in doped and undoped QWs with well widths from 10.5 to 3 nm, at energies from 210 to 535 meV. We observed a strong redshift of the absorption with increasing temperature. The size of the redshift increases with decreasing well width from 6.2 meV for the 10 nm sample to 12.0 meV for the 5 nm sample. A simple theory, taking into account only the temperature dependence of the effective mass and band offset, would predict a blueshift of the ISBA energy with increasing temperature. To explain these results correctly, we have developed a theoretical model based on the density matrix formalism. It incorporates all the major many-body effects via the semiconductor Bloch equations and nonparabolic subband dispersions via eight-band $\mathbf{k}\cdot\mathbf{p}$ calculations. Our model gives good agreement with the observed temperature dependence of the ISBA energy.

2 Sample Growth and Characterization

2.1 Sample structure

The samples were grown by molecular beam epitaxy (MBE) at Osaka Institute of Technology. The substrate was GaAs, and the buffer structure consisted of GaAs (300 nm) / AlAs (10 nm) / AlSb (100 nm) / GaSb (300 nm) / AlSb (1000 nm) / [AlSb/GaSb (6 nm / 6 nm)]x15 / AlGaSb (200 nm). The purpose of the thick buffer region is to compensate for the lattice mismatch between GaAs, with a lattice constant of 5.65 Å, and the 6.1 Å quantum wells. The active region consisted of 20 periods of InAs (x nm) / AlSb (10nm), where $x = 2.4$ to 10.5 nm. The active region was capped by 10 nm of GaSb or InAs to prevent oxidation of the AlSb. Most samples were not intentionally doped, but had a total electron density of 1.8×10^{12} to $6.9 \times 10^{13} \text{ cm}^{-2}$ at 77 K. We also well-doped some samples with Si. The wells were under tensile strain due to the 1.3% lattice mismatch between InAs and AlSb. Details of all of the samples grown are given in Section 7, Appendix B. In addition to single quantum wells, we grew several double quantum well (DQW) structures. They were grown on GaAs substrates and the buffer region described above. We grew two types: symmetric and asymmetric. The active region of the symmetric DQWs consisted of ten periods of undoped InAs (6.1 nm) / AlSb (x nm) / InAs (6.1 nm), where $x = 1.5, 1.2, 0.9,$ and 0.6 nm, separated by 10 nm AlSb barriers. The 77 K densities were 2 to $9 \times 10^{12} \text{ cm}^{-2}$. The asymmetric DQWs consisted of 10 periods of InAs (14.4 nm) / AlSb (0.9 nm) / InAs (5.8nm), separated by 20 nm AlSb barriers. One sample was doped and one was not.

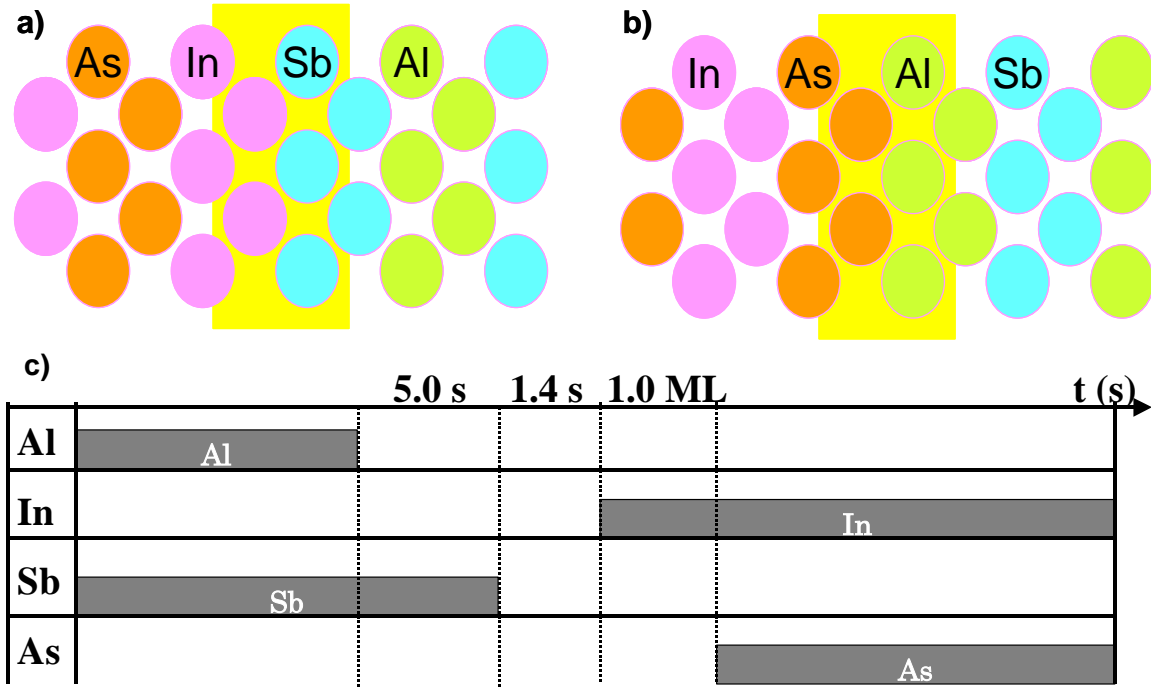


Figure 3: Two types of interface are possible in InAs/AlSb QWs: (a) InSb-like and (b) AlAs-like. The interface type is controlled by the MBE source shutter sequence. (c) shows the sequence for growing InSb-like interfaces.

We also grew several samples on GaSb substrates. These are attractive because the substrate is lattice matched to the heterostructure, so the crystal quality should be better than with GaAs substrates. In addition, the buffer region consists of only GaSb (200 nm) / AlGaSb (200 nm) and so GaSb-substrate samples are quick to grow. However, because semi-insulating GaSb substrates are not available, they cannot be used for transport measurements or far-infrared generation. We were not able to observe intersubband absorption in QWs grown on GaSb.

Two types of QW interface bonding are possible in this heterostructure: InSb-like and AlAs-like [Fig. 3(a), (b)]. Which one is grown is controlled by the MBE shutter sequence [Fig. 3(c)]. All of our samples were grown with InSb-like interfaces. InSb-like interfaces have been shown to give much stronger photoluminescence than AlAs-like, indicating better crystal quality.¹⁹ However, AlAs-like interfaces have been shown to

decrease the strain due to lattice mismatch, which is important in many-period structures such as quantum cascade lasers.²⁰ InSb-like interfaces also yield a higher electron mobility,²¹ which is not expected to affect the intersubband resonance significantly but does make transport measurements easier.

The growth was monitored *in situ* by reflection high-energy electron diffraction. The sample quality (period-to-period thickness uniformity) was evaluated by X-ray diffraction.

2.2 Transport measurements

2.2.1 Theory

We have characterized the electron concentration in these samples by Hall measurements and Shubnikov-de Haas (SdH) measurements.²²

The Hall effect was discovered by E. Hall in 1878. He applied a magnetic field perpendicular to a film of metal carrying a longitudinal current and observed a transverse potential V_H due to the deflection of the charge carriers by the Lorentz force. Figure 4 shows the Hall bar geometry, formed by selectively etching a two-dimensional electron gas (2DEG) and annealing contacts to it. In the Drude model, the forces on electrons due to external electric and magnetic fields are balanced by scattering according to

$e[\mathbf{E} + \mathbf{v}_d \times \mathbf{B}] = m\mathbf{v}_d / \tau$, where \mathbf{v}_d is the drift velocity of the electrons, m is the mass of an electron, and τ is the momentum relaxation time. For a two-dimensional metal, this

expression can be rewritten $\begin{pmatrix} E_x \\ E_y \end{pmatrix} = \frac{1}{\sigma} \begin{pmatrix} 1 & -\mu B \\ +\mu B & 1 \end{pmatrix} \begin{pmatrix} J_x \\ J_y \end{pmatrix}$, where the conductivity σ

$=en/\mu$, n is the areal density of electrons, the mobility $\mu = e\tau/m$, and J is the current

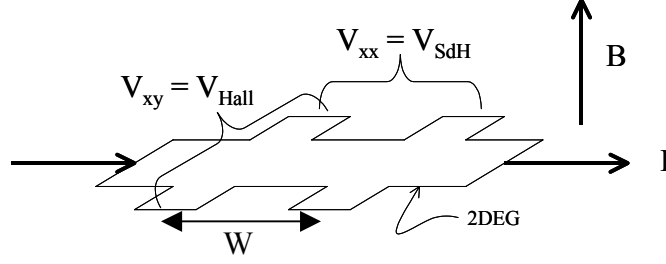


Figure 4: Hall bar geometry, showing magnetic field perpendicular to the 2DEG and potentials measured parallel and perpendicular to the applied current.

density per unit width. Then we can rewrite the above results in terms of the resistivity

tensor ρ , where $\mathbf{E} = \rho\mathbf{J}$, to get $\begin{cases} \rho_{xx} = 1/\sigma \\ \rho_{yx} = -\rho_{xy} = \mu B/\sigma = Be/n \end{cases}$. In equilibrium, the Hall

current $J_y = 0$, so $I = J_x W$ and the Hall voltage $V_H = V_{xy} = I\rho_{xy}$. The Hall voltage is proportional to the current and the applied magnetic field, and the sign of the Hall voltage indicates the sign of the charge carriers. The longitudinal voltage, V_{xx} , is a constant within this semiclassical model.

At high magnetic fields, the longitudinal voltage exhibits oscillations as a function of magnetic field. These oscillations were first observed by Shubnikov and de Haas in bulk metals in the 1930's. The Shubnikov-deHaas (SdH) oscillations arise due to Landau quantization of the electron system in a strong magnetic field. Let us consider a 2D system for simplicity. The Landau level energies of a 2DEG in a perpendicular magnetic field are $E = E_z + (n + \frac{1}{2})\hbar\omega_c + g\mu_B B_z$, where E_z is the energy of the lowest subband due to confinement in the growth direction, $\omega_c = eB/m^*$ is the cyclotron frequency, m^* is the cyclotron effective mass, the n and $n+1$ levels are separated by the cyclotron energy of $\hbar\omega_c$, g is the effective g-factor, μ_B is the Bohr magneton, and $g\mu_B B_z$ is the spin splitting energy. In InAs, the electron effective mass is $0.026 m_0$ and $g = -14.8$ at the band edge.

Landau quantization causes the density of states (DOS) of the 2DEG, which is independent of energy in the absence of magnetic fields, to become peaked at the Landau level energies. The sharpest peaks occur in low-disorder 2DEGs at low temperature and high magnetic field.

The filling factor of the system describes the number of Landau peaks below the Fermi energy E_F . It is given by $\nu = \frac{n}{N} = \frac{hn}{eB}$, where n is the areal density of electrons and N is the degeneracy of a Landau level. For example, when $\nu = 3.5$, the lowest three spin split Landau levels are completely full and the fourth is half full, so μ lies in the fourth Landau levels. The Fermi energy lies in the middle of a cyclotron gap (spin gap) when the filling factor is an even (odd) integer. For higher magnetic fields, ν is smaller and the Landau levels are farther apart.

SdH oscillations occur when E_F moves through the Landau levels. This can happen by changing either the magnetic field (this experiment) or the charge density (*e.g.* Si-MOSFET). As E_F moves through the Landau levels, the DOS at the Fermi energy changes. The longitudinal resistance, ρ_{xx} , has peaks when the Fermi energy is in the center of a Landau level because at that energy, there are the most states available for scattering of the current. The Hall resistance, ρ_{xy} , also oscillates, with a larger slope at peaks in the DOS due to more scattering and plateaus between them. Figure 5 shows a typical SdH trace of longitudinal resistance vs. magnetic field for our samples.

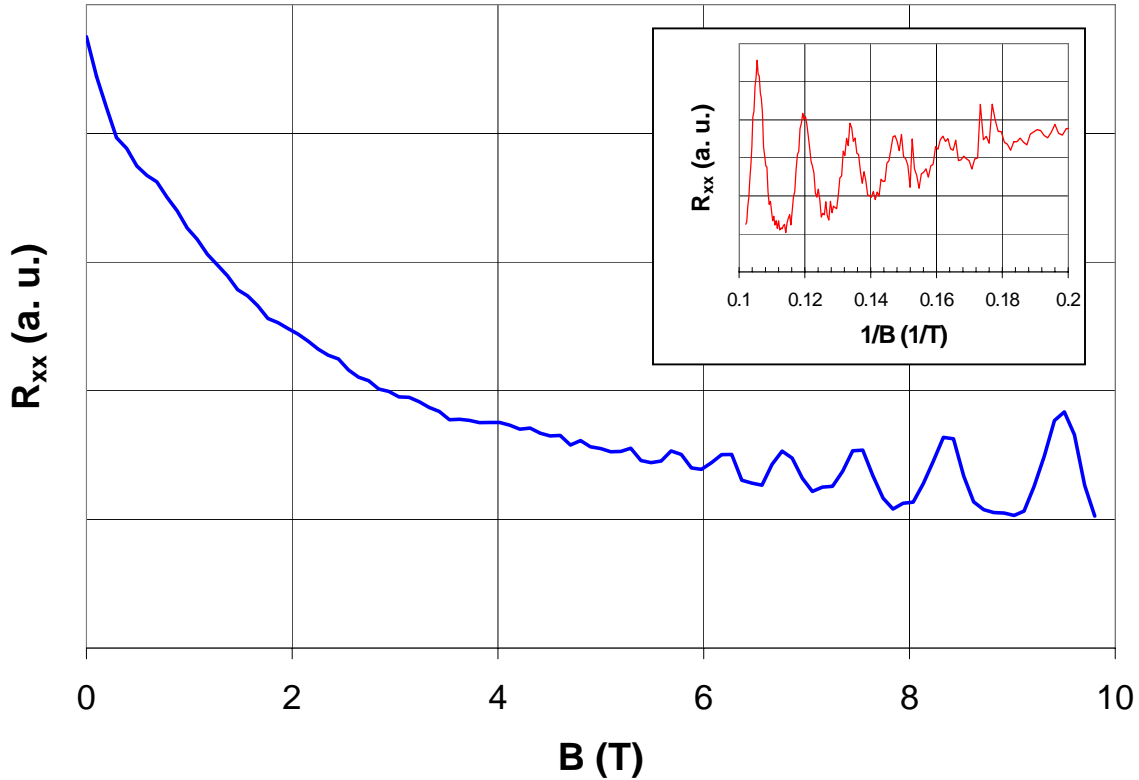


Figure 5: Shubnikov-deHaas oscillations in the longitudinal resistance of sample D at 1.6 K. The inset shows the resistance as a function of $1/B$.

So how do you extract the density from SdH traces? Recall that $\nu = \frac{hn}{eB}$. You

can use this to figure out the filling factors of a set of valleys by noting that a valley at a high magnetic field will have a companion valley at half the magnetic field but with twice the filling factor. By counting the number of valleys in between this pair (ignoring valleys due to spin-splitting), you can unambiguously identify the set. To find the density, plot the filling factor as a function of $1/B$, and the slope gives the density.

How high does the magnetic field need to be for Landau levels to form? It should be high enough for an electron to complete at least a few orbits before scattering:

$1/\omega_c \ll \tau$, or $B \gg 1/\mu$. So, to see clear oscillations in a magnetic field of 10 T, the

mobility should be around $100,000 \text{ cm}^2/\text{Vs}$, which is what we observe. This is why SdH

oscillations cannot be observed in low-mobility 2DEGs. SdH oscillations also require a sharp Fermi edge, *i.e.* $\hbar\omega_c \gg k_B T$. For $T = 1.8$ K, this corresponds to ~ 5 T.

In our measurements, we use the Van der Pauw geometry rather than a Hall bar. Van der Pauw showed that Hall measurements could be made on 2D films of arbitrary shape with four contacts by applying current and measuring voltage in all possible combinations of directions across the contacts, with and without an applied magnetic field, then taking weighted averages.²³ The averaging procedure eliminates errors that arise when, for example, the line between the contacts measuring V_H is not perpendicular to the applied current. In addition, this four-contact method eliminates error due to the contact resistance because the voltage is measured across a separate pair of contacts from the current application. The Van der Pauw method greatly simplifies sample fabrication.

The sample is prepared by annealing small pieces of indium at the corners of a square sample. The indium diffuses into the semiconductor and makes electrical contact with the two-dimensional electron gases in the quantum wells. In both techniques, a magnetic field is applied to the sample along the growth direction, a small current (~ 1 μ A) is applied across the sample, and the voltage is measured across the other pair of contacts. For low-field Hall measurements, the applied magnetic field is around 0.1 T (1000 G) from a small permanent magnet. For low-field Hall measurements, we apply the Van der Pauw method to find the room temperature and 77 K density and mobility of each sample. For SdH measurements, we apply a magnetic field of up to 10 T using a superconducting magnet. In this case, the density comes from the magnetic field position of the valleys, which is not affected by the size or shape of the sample or the resistance of the contacts.

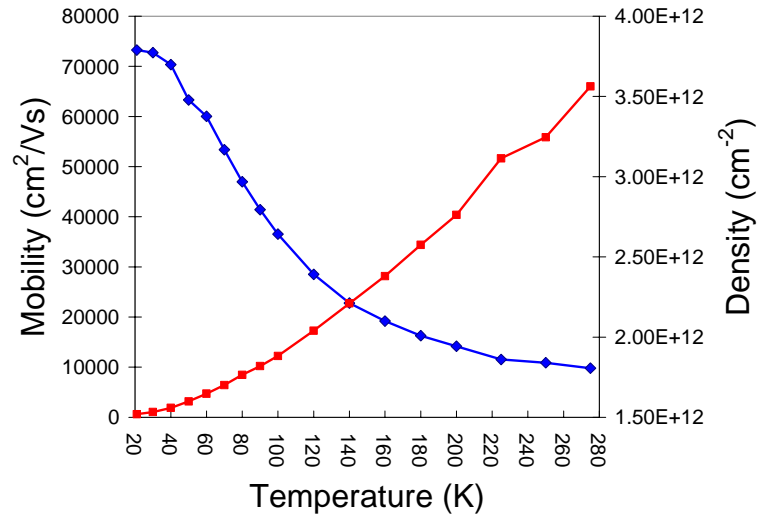


Figure 6: The temperature dependence of the mobility (left axis, blue diamonds) and Hall density (right axis, red squares) of sample F.

These two techniques give complementary information. Low-field Hall measurements are sensitive to the total carrier concentration in the sample, including all populated QWs as well as any free carriers in the buffer or substrate. Because semi-insulating GaSb substrates are not available, it would therefore be more difficult to measure the concentration of QWs grown on GaSb using the Hall effect. SdH measurements are sensitive only to high mobility 2DEGs, not buffer or substrate carriers. Individual 2DEGs in the same sample but with different densities will have different SdH periods. The combination forms a characteristic beating pattern in the SdH trace.²⁴

2.2.2 Temperature-dependent Hall measurements

We have made temperature-dependent Hall measurements of sample F, shown in Fig. 6. The total density increases with temperature and the mobility decreases as expected due to thermal ionization of donors. Most of the temperature dependence of the density is believed to come from interface donors.²⁵

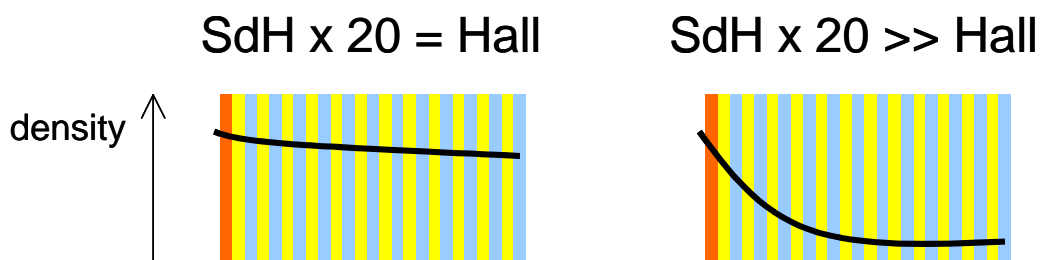
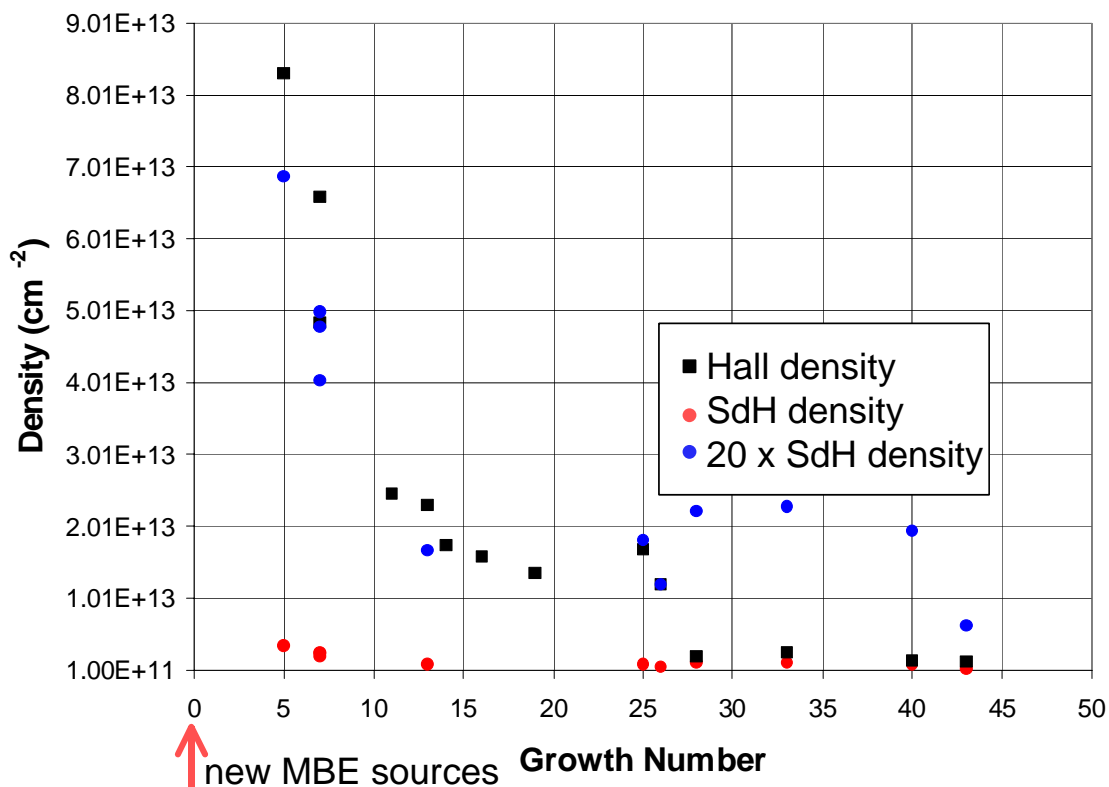


Figure 7: The total, Hall density (black squares), the single-well, Shubnikov-de Haas density (red circles), and 20 times the SdH density (blue circles) for a variety of InAs/AlSb QWs as a function of the number of growths since the MBE sources were replaced. The cartoons below show the inferred density profile through the sample for low and high growth numbers.

2.2.3 Carrier distribution

We observe two regimes of sample population in our not-intentionally-doped QWs, as shown in Fig. 7. Wells grown early in the MBE run have Hall densities equal to about 20 times the SdH density. This indicates that all the wells are about equally

populated. Wells grown late in the run have Hall densities approximately equal to the SdH density, showing that only about one well is populated. The most likely sources of electrons in these wells are bulk²⁶ and interface^{25,27} donors and Fermi level pinning at the surface of the GaSb cap layer,²⁸ ~500 meV above the InAs conduction band.²⁹ We attribute the large variation in total electron density to variation in the density of bulk donors, which are initially present in the chamber but are removed during the run. So, the early grown samples are dominated by bulk donors, while the late grown samples are populated primarily by Fermi level pinning at the GaSb surface.

For the best control of the carrier density and distribution, the growth should:

1. wait until the density of bulk donors is low
2. dope the QWs with Si to control the density
3. cap the structure with InAs instead of GaSb for minimal band bending

In the InAs cap layer, the Fermi energy is pinned 80 meV above the InAs conduction band, causing less band bending and hence nonuniformity in the energy band profile and carrier distribution. We have begun to implement the above steps; the results will be detailed in the section on intersubband absorption.

2.3 Cyclotron resonance

Cyclotron resonance^{30,31,32} (CR) measures band parameters in semiconductors such as effective masses. The resonance is detected by applying a magnetic field and measuring the transmission of light through the sample while varying the wavelength of the incident probe light and/or the magnetic field. The resonance energy is proportional to the applied magnetic field \mathbf{B} according to $\omega_c = eB/m^*$, where m^* is the effective mass

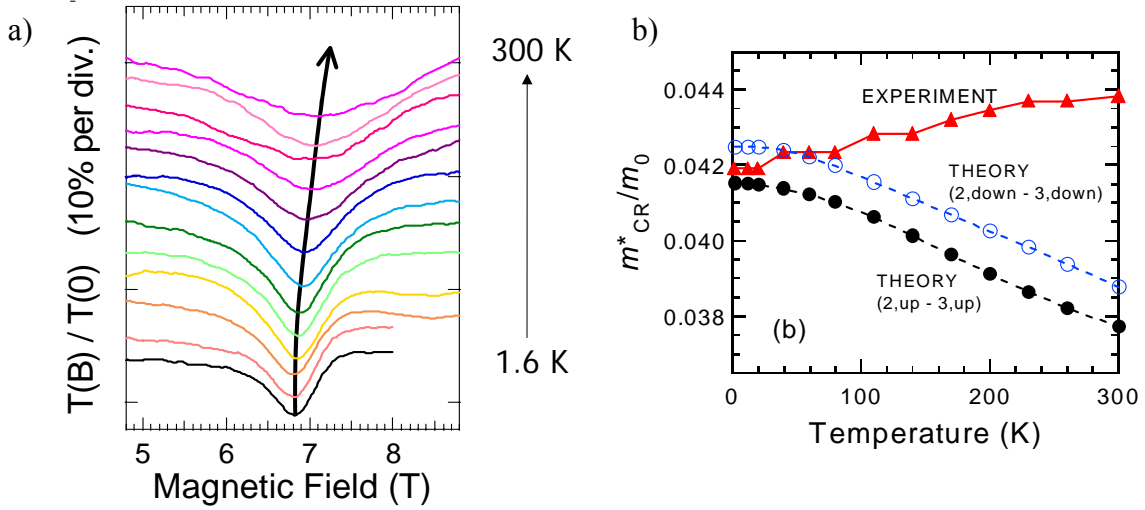


Figure 8: (a) Cyclotron resonance using a 4.7 THz QCL in sample F at various temperatures from 1.6 to 300 K. (b) Calculated (circles) and experimental (triangles) values of the effective mass as a function of temperature for sample F.

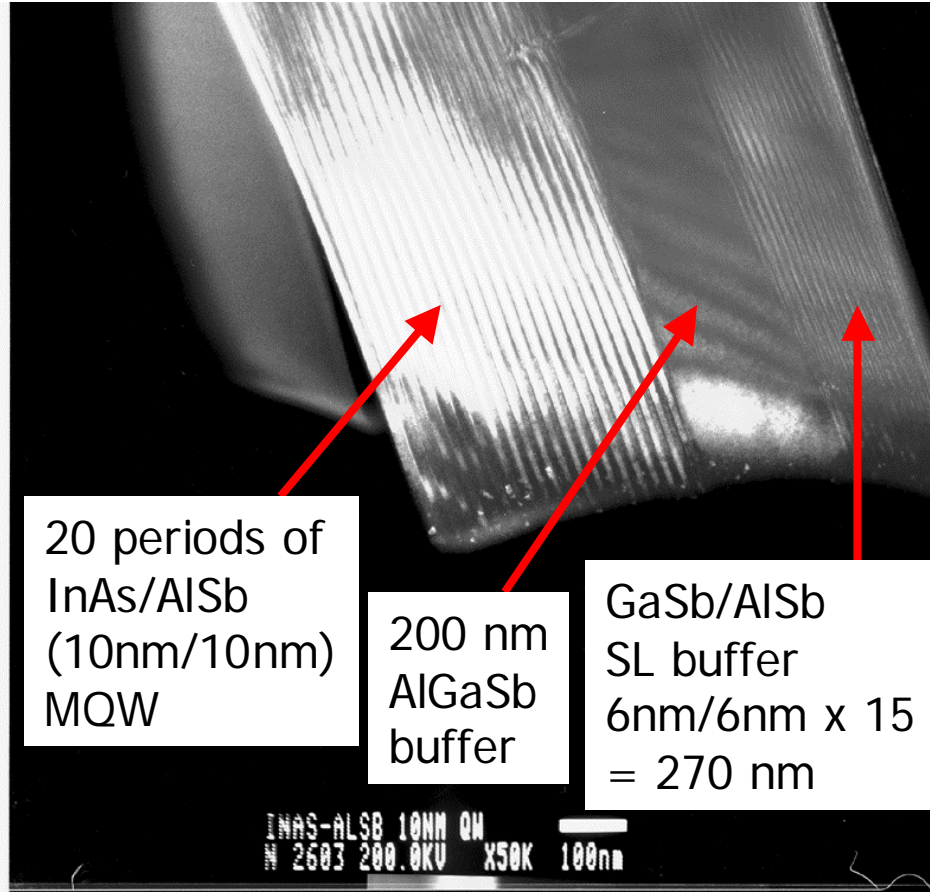
of the charge carriers. The temperature dependence of the effective mass is a useful parameter for modeling temperature dependent intersubband resonances.

We have measured CR in sample F using a THz quantum cascade laser as the light source.³³ The QCL emitted at 4.7 THz (64 μm) with a maximum CW power of ~ 4 mW.³⁴ The QCL was operated at 135 Hz with a duty cycle of 25%. The light was transmitted through a magnet with z-cut quartz windows and detected with a liquid-helium-cooled Si bolometer. The entire beam path was purged with dry nitrogen. The short-term wavelength drift was ~ 20 MHz over 30 s, measured by beating with a THz gas laser.³⁵ Any long-term drift was unnoticeably small during the CR measurement. The short-term intensity fluctuations were $\sim 0.5\%$ over 1 s; long-term drift was dominated by humidity fluctuations in the beam path. The sample was twenty periods of InAs/AlSb quantum wells, with a total electron density of $1.2 \times 10^{12} \text{ cm}^{-2}$ and a mobility of $120,000 \text{ cm}^2/\text{Vs}$.

Figure 8(a) shows the QCL transmission as a function of magnetic field from 1.6 to 300 K. The resonance shifts to higher magnetic field and broadens with increasing temperature. Figure 8(b) shows the cyclotron mass, corresponding to the peak position, as a function of temperature from 1.6 to 300 K.

As shown in Fig. 8(b), the cyclotron mass increases with increasing temperature.³⁶ This is opposite to the expected behavior: as the band gap decreases with increasing temperature, the effective mass should *decrease* due to the increased coupling between the conduction and valence bands. Two calculated curves are also shown in Fig. 8(b) to highlight this unexpected behavior. These curves correspond to the (2,up) to (3,up) and (2,down) to (3,down) transitions, where the number is the Landau level and the orientation is the spin direction. These transitions are expected based on the density and eight-band $\mathbf{k}\cdot\mathbf{p}$ calculations. The temperature-dependent effective masses for these transitions are calculated via a modified Pidgeon-Brown model³⁷ including strain, quantum confinement, and the temperature dependence of the band gap. The CR line is fairly broad at high temperatures and it is likely that higher-level CR transitions (e.g., 3 to 4) are involved, contributing to the higher masses. Although this thermal population of higher levels could certainly shift the center-of-gravity of the peak to higher magnetic fields (i.e., higher masses), the important fact is that there is no sign of a red shift of the peak even in the temperature range where the linewidth remains nearly the same (up to ~ 80 K). Our calculations show that *all* cyclotron masses must decrease with increasing temperature no matter which transitions are involved. A more comprehensive model is necessary to explain this behavior.

a)



b)

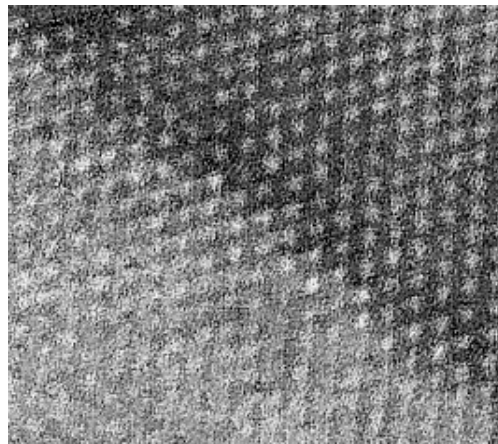


Figure 9: Transmission electron micrographs of a 10 nm InAs/AlSb QW. (a) Low-resolution image showing QWs and part of the buffer region. (b) Atomic resolution image showing interface between InAs and AlSb.

2.4 TEM

We have made preliminary high-resolution cross-sectional transmission electron microscope measurements of the QW samples, shown in Fig. 9.³⁸ The purpose of cross-sectional measurements is to characterize the QW interface roughness. Interface roughness scattering (IFRS) is a significant broadening mechanism in ISBAs.³⁹

2.5 Photoluminescence

We have measured photoluminescence (PL) in InAs/AlSb QWs, as shown in Figure 10. The pump source was an Ar⁺ laser ($\lambda = 514 \text{ nm} = 2.4 \text{ eV}$), and the sample was at low temperature. The PL energy is consistent with the indirect transition between the lowest energy quantized states from the InAs CB to the AlSb VB. The PL is stronger for narrower wells, as expected because the hole states in the AlSb layers penetrate further into the narrow barrier presented by InAs. This increases the spatial overlap between the electron and hole states, increasing the optical matrix element of the transition.

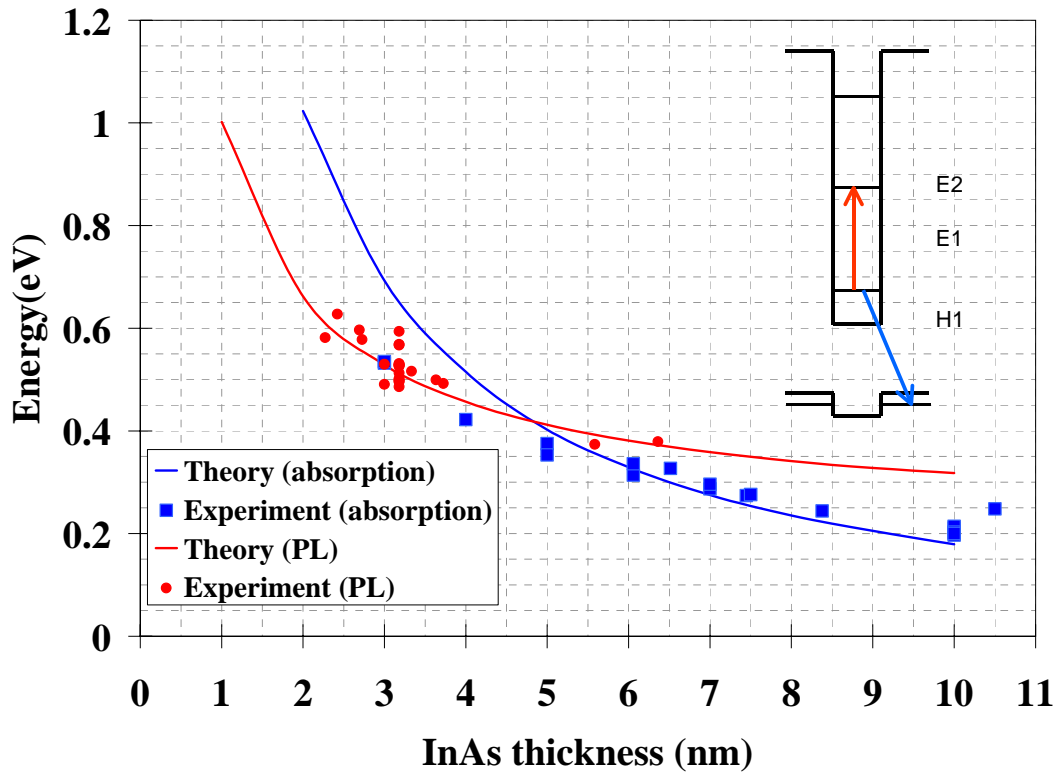


Figure 10: Photoluminescence energy (red circles) and ISBA energy (blue squares) as a function of well thickness for InAs/AlSb quantum wells. The lines show the PL and ISBA energies calculated using a simple single-particle model. The inset shows the energy levels involved in PL and ISBA.

3 Intersubband Absorption

3.1 Selection Rules and Experimental Geometry

We detect the ISBA via its polarization selection rule. Light is absorbed or emitted by the intersubband resonance only when it is polarized in the growth direction, z .⁴⁰ Classically, the polarization selection rule arises because the strong z direction confinement makes the electrons bounce around in the z direction much faster than in x and y , creating oscillating dipoles in the z direction which can radiate and absorb only radiation polarized along z . Quantum mechanically, the dipole matrix element is nonzero only for light polarized along z :

$$\begin{aligned} \langle f_i | \mathbf{E} \cdot \mathbf{p} | f_f \rangle &= \int d^3r \chi_{n_i}^*(z) e^{-i\mathbf{k}' \cdot \mathbf{r}} [E_x p_x + E_y p_y + E_z p_z] \chi_{n_f}(z) e^{i\mathbf{k} \cdot \mathbf{r}} \\ &= (E_x \hbar k_x + E_y \hbar k_y) \delta_{n_i, n_f} \delta_{\mathbf{k}', \mathbf{k}} + E_z \delta_{\mathbf{k}', \mathbf{k}} \int dz \chi_{n_i}^*(z) \left(-i\hbar \frac{\partial}{\partial z} \right) \chi_{n_f}(z) \end{aligned}$$

The first term describes Drude absorption ($\omega = 0$), which is allowed only for light polarized in the 2DEG plane. The second term describes intersubband absorption, which for finite frequencies occurs only for light polarized perpendicular to the 2DEG.

Although many experimental efforts have been made to violate the polarization selection rule, the general consensus is that it is a strong rule for the conduction band. In the valence band, normal incidence ISBA is possible due to the complexity of the bands.⁴¹

In the expression for the intersubband dipole matrix element, the $\chi_n(z)$ are the envelope wavefunctions of the QW states. In the infinite barrier approximation, the $\chi_n(z)$ are given by:

$$\chi_n(z) = \begin{cases} \cos\left(\frac{n\pi z}{L}\right) & \text{for } n \text{ odd} \\ \sin\left(\frac{n\pi z}{L}\right) & \text{for } n \text{ even} \end{cases}$$

for a well of width L , centered at $z = 0$. By applying these wavefunctions to the dipole matrix given above, it can be seen that the matrix element for intersubband transitions is nonzero only when $\Delta n = 1$. This is the intersubband energy level selection rule.

The simplest way to couple light to the ISBA is by putting the sample at an angle to the incident beam, as shown in Fig. 11. However, because the allowed component of the beam is small in this geometry, the ISBA signal is weak. In order to couple light to the intersubband resonance more strongly, we use the parallelogram geometry. The sample is polished at 45° and the light beam is incident normal to the polished face. In this geometry, s -polarized light cannot be absorbed by the intersubband resonance but half of a p -polarized beam can be absorbed. A similar strong coupling geometry is the trapezoid.

We also coated the QW surface with 100 nm of gold. This treatment is expected to make light beam's electric field have an antinode rather than a node at the QW surface, increasing the coupling to the QWs.⁴² We have compared coated and uncoated QWs. We observed the same absorption intensity and a small shift in energy (~ 2 meV higher when uncoated). All of the samples discussed here are coated.

The intersubband absorption was measured with a Fourier transform infrared spectrometer. We used a Jasco FTIR-660 with a spectral range of 15,000-100 cm^{-1} (666 nm – 100 μm) and a resolution of 16-0.25 cm^{-1} . It is a continuously scanning instrument with a vacuum interferometer, automatic beamsplitter alignment, and a mid-infrared

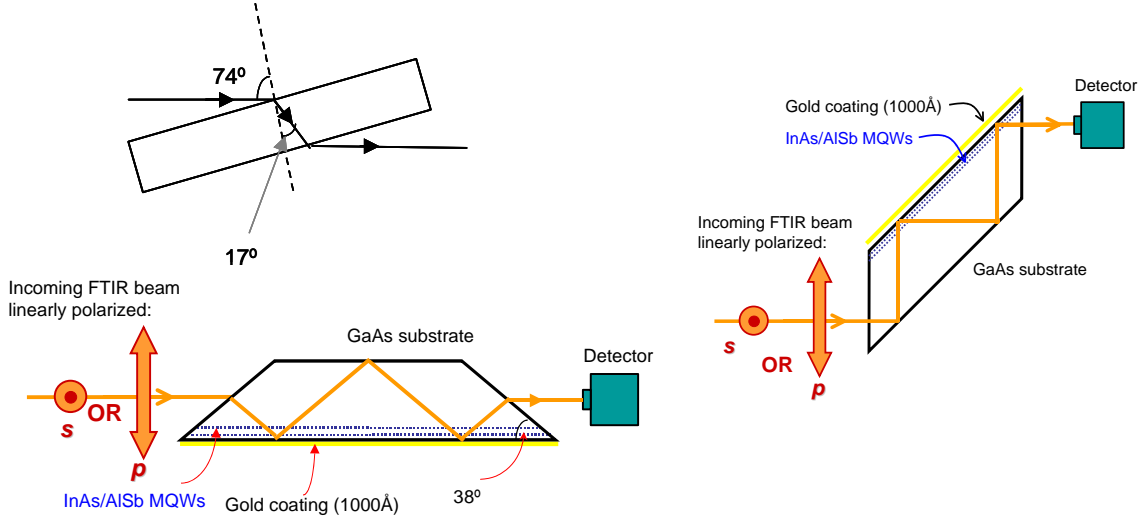


Figure 11: Three common experimental geometries for the observation of ISBA. Counterclockwise from top left, the Brewster angle geometry with unpolarized incident beam, the trapezoid geometry, and the parallelogram geometry (this work).

microscope attachment. The sample was placed in a helium-flow cryostat, a wire grid polarizer was placed before the sample, and the beam path was purged with nitrogen. In order to detect the resonance, we took the ratio of the p -polarized light to the s -polarized light (intersubband active to inactive). In order to cancel out background differences in the transmission of s - and p -polarized light, we also took the s/p ratio of an empty aperture in the same shape and position of the sample. So, the final spectrum was

$$T = \frac{\left[\frac{T_p}{T_s} \right]_{\text{sample}}}{\left[\frac{T_p}{T_s} \right]_{\text{empty}}}.$$

The absorption coefficient of the sample, α , was calculated as

$\alpha = (-\ln(T) + R) / L$, where R is a sample- and temperature-dependent constant chosen to make α equal zero away from the absorption, and L is the total length of well material that the infrared beam passes through.

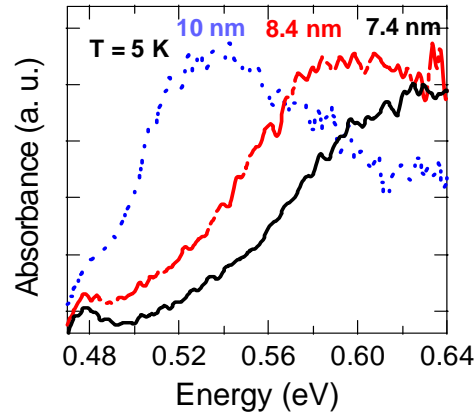


Figure 12: *S* polarized interband spectra at 5 K are shown, normalized to a sample without quantum wells. The 10, 8.4, and 7.4 nm well widths are samples A, C, and B. The interband absorption edge shifts to higher energy with decreasing well width. The *p* polarized interband spectra are similar.

3.2 Interband absorption

Figure 12 shows the *s* polarized interband absorption spectra of samples A, C, and B (10, 8.4, and 7.4 nm well width). These samples have both interfaces InSb-like and are undoped. The interband spectra are the ratio of the sample transmission at one polarization to the transmission of a reference sample, grown without quantum wells, at that polarization. The figure shows $\ln\left[T_s^{sample} / T_s^{reference}\right]$, i.e. absorbance, versus energy. The interband absorption edge shifts to higher energy as the well width decreases, mainly due to the increase in energy of the lowest quantized state in the well. Prevot *et al.* have observed similar spectra in 6.5 to 8.5 nm InAs/AlSb wells.⁴³ They also observe a difference between the shapes of the *s* and *p* polarized interband absorptions below the interband peak which is not present in our data.

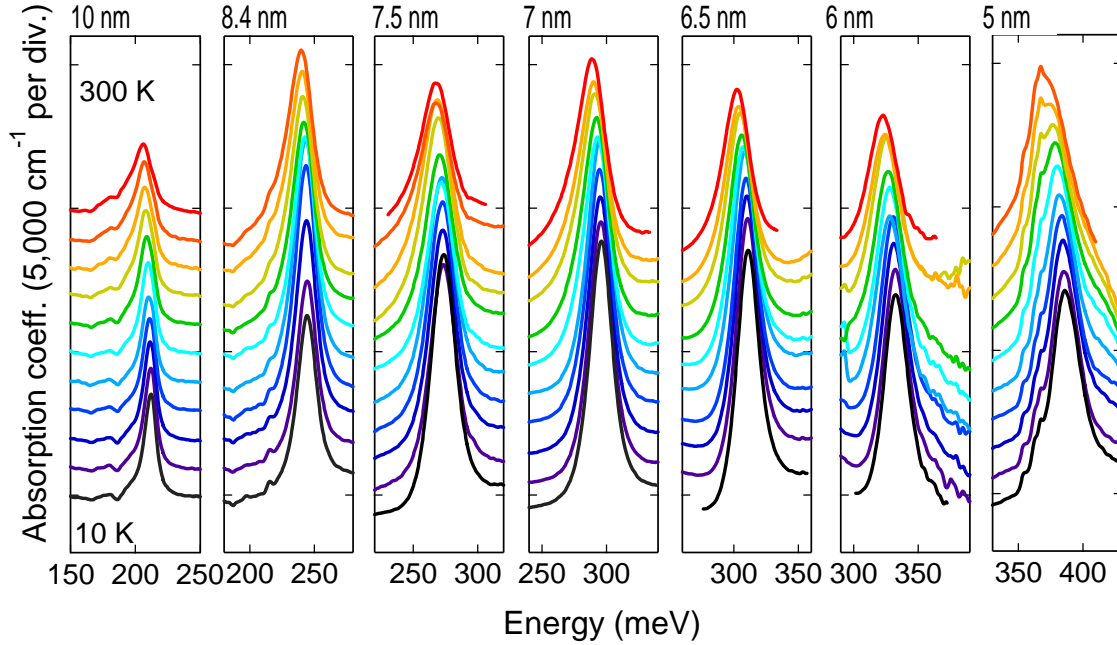


Figure 13: Intersubband absorption spectra of InAs/AlSb QWs (from left to right, samples A, D, B, J, K, L, and M). The absorption coefficient is plotted as a function of energy from 10 K to 300 K.

3.3 Temperature dependence of ISBAs in medium-density wells

Figure 13 shows the intersubband absorption spectra of QWs with widths from 10 to 5 nm (samples A, D, B, J, K, L, and M) from 10 K to 300 K. These samples have roughly the same total electron density, around $1 \times 10^{13} \text{ cm}^{-2}$, and a per well density of about $1 \times 10^{12} \text{ cm}^{-2}$. For this per well density, only the lowest subband is populated. The absorption coefficient of the sample, α , is plotted versus energy. The ISBA energy increases with decreasing well width from 212 meV ($5.84 \mu\text{m}$) for 10 nm wells to 385 meV ($3.22 \mu\text{m}$) for 5 nm wells at 10 K. For a given well width, the ISBA peak position redshifts with increasing temperature. The amount of redshift increases with decreasing well width from 6.2 meV for 10 nm to 12.0 meV for 5 nm, as shown in Fig. 14(a). Similar, but much smaller, redshifts have been reported for ISBAs in GaAs/AlGaAs

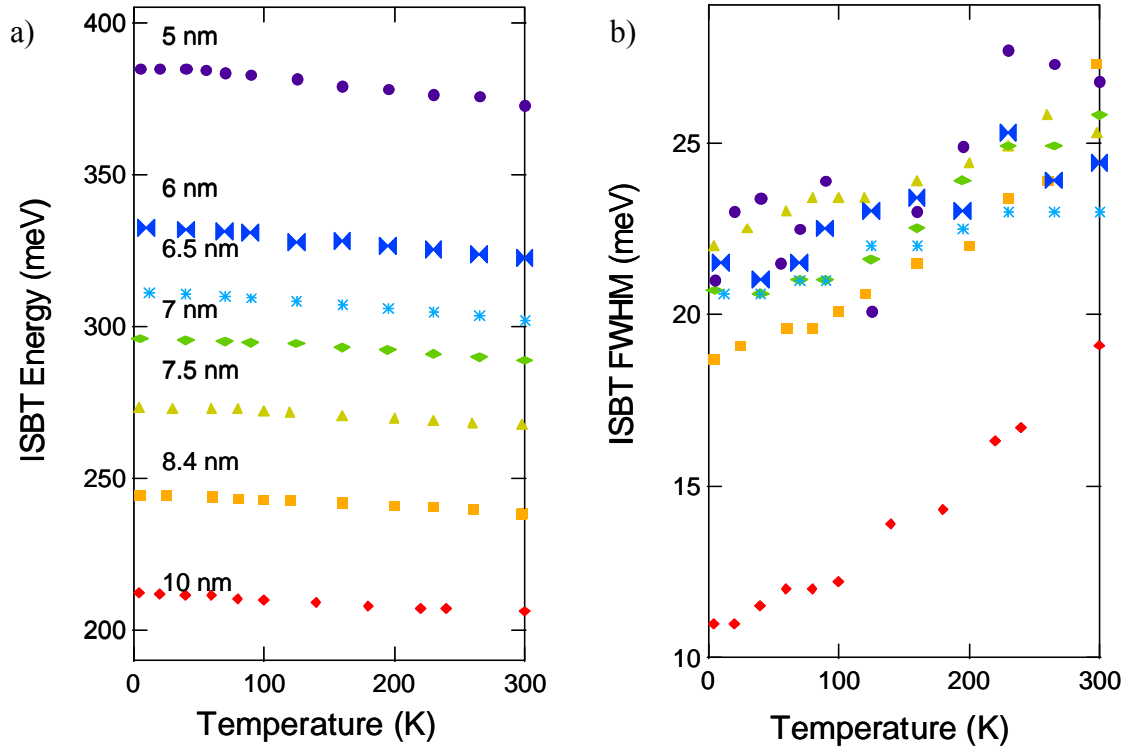


Figure 14: Temperature dependence of intersubband transition (a) peak energy and (b) full-width at half maximum for the samples in Fig. 12.

quantum wells.^{44,45,46} The ISBA linewidth has a weak temperature dependence, increasing from 10 K to 300 K by a factor of less than 2, as shown in Fig. 14(b). The low temperature linewidths are relatively small, ranging from 11 to 23 meV (2.8 to 5.8 THz), indicating that the interface type and smoothness are well controlled. The ISBA linewidth does not vary systematically with well width.

3.4 Electron density and distribution—comparison of 10 nm

QWs

We have grown many nominally 10 nm QW samples which illustrate the strong effects of the electron density and distribution on the ISBA. The energy of the resonance

in these samples varies unsystematically with density. We attribute the energy variation of ± 6 meV to a well thickness variation of ± 0.2 nm (less than one monolayer). All of the spectra shown were taken at 77 K.

3.4.1 Low vs. high density

Figure 15(a) shows the ISBA of one high density and two low-density samples. The absorption coefficients are scaled to the same peak amplitude in order to compare the lineshapes. The high-density sample (H) has all wells about equally populated, and the low-density samples (A, F) have only about one well heavily populated. The SdH density of the high-density sample is about twice that of the low-density samples. The full width at half maximum (FWHM) of the high-density sample is 22 meV, whereas for the low-density samples it is 12 and 12.5 meV. Mono-layer fluctuations in the well width, either between layers or within a single layer, would cause inhomogeneous broadening of about 8 meV. But this broadening mechanism should be the same in all three samples. A more likely source of increased broadening in the higher density sample is increased depolarization shift, a many-body effect discussed in Sec. 4.2.2, which in this regime of well width and density broadens and blueshifts the resonance.⁴⁷

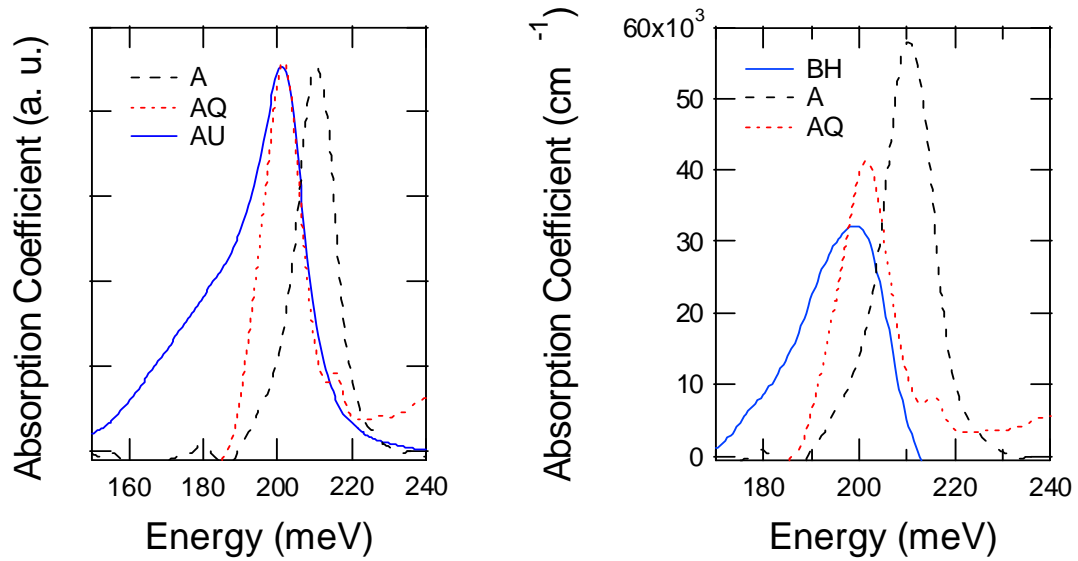


Figure 15: Intersubband absorption spectra comparing samples with (a) low (A, F) and high (H) total density and (b) one (N) and twenty (A, F) QWs, as described in the text.

3.4.2 Single vs. multiple wells

In order to investigate the effects of well-to-well width fluctuations, we grew a sample with only one QW (sample N). Figure 15(b) shows the ISBA of the single QW sample and the two low-density samples of Fig. 15(a), which have only a few wells populated. The absorption coefficients of the low-density multi-well samples in this figure are calculated assuming one well is populated. The single well's density is about the same as the single well densities of the multi-well samples. However, the single well's FWHM is 19.5 meV, almost twice as wide as the multi-well ISBAs. This result is surprising. We expected the single well ISBA to be at least as narrow as the low density ISBAs because the ISBA broadening mechanisms are all about the same. The single well should have about the same degree of band bending, the same amount of interface roughness scattering, the same many-body effects, and of course the same degree of

nonparabolicity. The discrepancy may arise because of large variations in the baseline of sample N, as described in Sec. 3.9.2.

3.4.3 InAs vs. GaSb cap

In order to reduce band bending at the sample surface to make the charge distribution more homogeneous, we have capped some samples with InAs rather than GaSb. The Fermi level is pinned ~ 80 meV above the InAs CB at an InAs surface, rather than ~ 500 meV at a GaSb surface. So, the InAs cap layer causes less band bending. In Fig. 16(a) we compare samples grown with a GaSb and an InAs cap (samples H and Q). The comparison is not ideal because the total density of the GaSb capped sample is three times larger than the InAs. However, the sample with the GaSb cap has a more asymmetric lineshape, indicating more inhomogeneous broadening. This could be due to increased nonparabolicity effects in the higher-density, GaSb-capped sample, or reduced band bending in the InAs-capped sample. Band bending in QWs near the surface changes the shape of the QW potential, changing the energy level separations compared to deeper QWs and so causing inhomogeneous broadening. We have not yet made SdH measurements in the InAs-capped sample to confirm the improved charge uniformity.

3.4.4 Thick vs. thin AlSb top barrier

Another way to reduce the band bending caused by surface Fermi level pinning is to increase the top AlSb barrier thickness. We tried this in one sample (G), and found from density measurements that the charge distribution is indeed more uniform than in a similar sample with a 10 nm AlSb top barrier (F). It is not clear whether the reduced band bending affects the ISBA, however [Fig. 16 (b)]. G has a slightly narrower

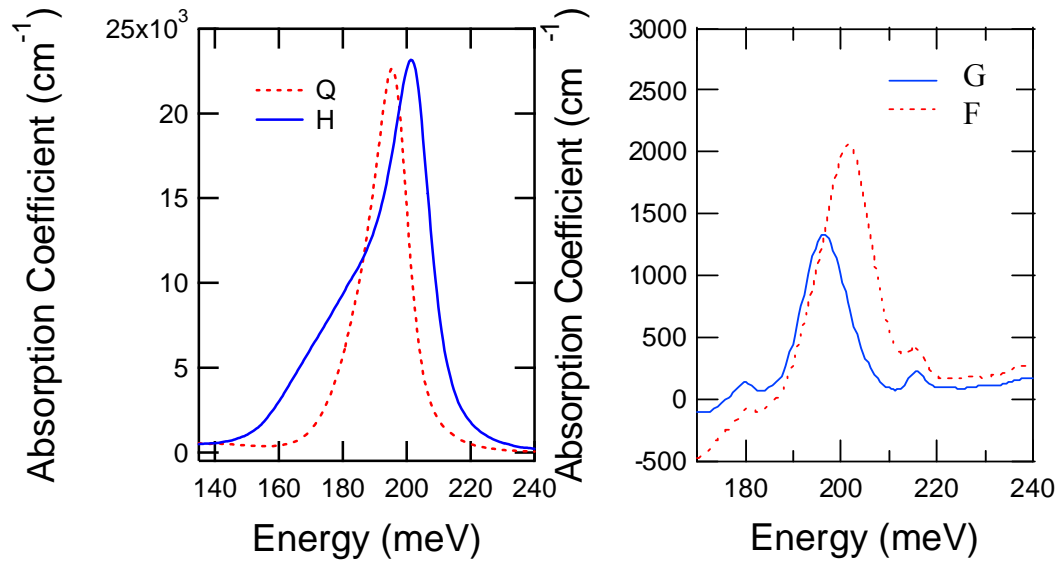


Figure 16: Intersubband absorption spectra comparing samples with (a) InAs (Q) and GaSb (H) cap layers, and (b) thick (G) and thin (F) top AISb barriers, as described in the text.

resonance than F (11 meV vs. 12.5 meV FWHM), but this may be due to the smaller per-well density in G.

3.5 Doping

In addition to reducing band bending, we have controlled the carrier distribution by doping. Doping inside the well is necessary in this structure: the only donor which could be put in the AISb barrier is Te, but this element contaminates later MBE growths. Doping in the well reduces the 2DEG mobility. It has been shown that well doping also increases the ISBA linewidth compared to remote doping.⁴⁸ The ISBA linewidth is influenced primarily by collective effects and scattering off interface roughness; ionized impurities and phonons are less important.^{39,49} We have not systematically studied the effects of doping on our ISBAs. However, it does not dramatically increase the linewidth.

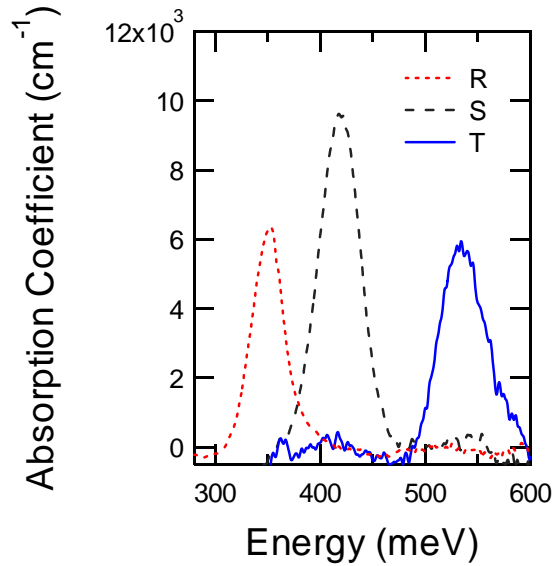


Figure 17: High energy intersubband absorption spectra showing narrow absorption peaks despite doping and stronger interface roughness scattering.

3.6 High energy ISBA

We have observed ISBA in wells as narrow as 3 nm. Figure 17 shows the absorption coefficients of 5, 4, and 3 nm QWs (samples R, S, and T). The ISBA energies are 353, 420, and 535 meV at 77 K, with FWHMs of 36, 44, and 51 meV. The key to observing these resonances is a high carrier density, which we achieved by well doping with Si to $\sim 2.5 \times 10^{12} \text{ cm}^{-2}$ per well ($5 \times 10^{13} \text{ cm}^{-2}$ total density).

Is NIR ISBA feasible in this material system? The highest energy ISBA which has been reported in InAs/AlSb QWs is 626 meV (1.98 μm) with FWHM = 60 \pm 10 meV, in 2.7 nm Si doped QWs by Ohtani *et al.*⁵⁰ We are investigating 2 and 1.5 nm QWs but have not yet seen any ISBA. We expect to be able to do so because the ISBA in our slightly wider wells is narrow and strong. The broadening of the ISBA due to increased IFRS should not be enough to destroy the ISBA in the narrowest wells. However, the higher energy absorption will be more difficult to observe experimentally because of

interband absorption in the InAs QWs and, at even higher energies, in the GaSb/AlSb buffer superlattice.

Does interband absorption impede intraband absorption? No. Ohtani *et al.* have observed strong ISBA in 3.3 and 2.7 nm QWs at 545 and 626 meV, about 25 meV above their respective PL energies. Interband absorption at high energies (Ar⁺⁺ laser = 3.5 eV) has also been used to modulate the QW population and detect the ISBA.⁵¹ Limitations of a NIR ISBA as a pumping resonance for THz emission may include three-dimensional free carrier absorption in the thick GaSb buffer layer and lattice heating created by interband absorption.

3.7 Un-like interfaces

When there is an asymmetric electric field in the QW growth direction, the 2DEG sees an effective magnetic field. The asymmetry may be provided by the bulk inversion asymmetry of the crystal⁵², structural inversion asymmetry (SIA) such as asymmetric doping⁵³ or an applied electric field^{54,55}, or native interface asymmetry (NIA) such as different interfaces on opposite sides of the QW⁵⁶. The effective magnetic field lifts the spin degeneracy of the subbands, adding an extra term to the Hamiltonian

$H_{so} = \alpha(\boldsymbol{\sigma} \times \mathbf{k}) \cdot \mathbf{z}$, where α is the spin-orbit coupling constant, $\boldsymbol{\sigma}$ is the Pauli spin matrix, and \mathbf{z} is the QW growth direction. The dispersion relation gains a wavevector-dependent term $\pm \alpha k_x$. These effects are expected to be large in narrow gap III-V semiconductors such as InAs and InSb, which have very large spin-orbit coupling.

Spin splitting due to SIA is known as the Rashba effect. It is typically a few meV and is inferred from low-field magnetoresistance measurements, where beating in the SdH trace indicates two populated subbands.^{53,54,55} Splitting of the hole subbands due to

SIA has also been observed by intersubband absorption measurements in Si inversion layers.⁵⁷

In heterostructures with no common atom between layers, such as InAs/AlSb, it is possible to grow two different types of interfaces. A QW with asymmetric interface types, or NIA, is predicted to show Rashba splitting due to the asymmetric potential felt by the well. This effect is estimated to be a few meV in wells of a few nm width. We have grown several samples of 10 nm QWs with one interface InAs-like and one AlSb-like. Samples D and E show large splittings, ~ 30 meV. However, we are dubious about the composition of these samples because their ISB resonance energies are higher than in any other 10 nm QW. Another 10 nm sample with unlike interfaces, sample I, shows a slight asymmetry which might indicate a splitting of ~ 20 meV. However, a 10 nm sample with a similar density but like interfaces, sample H, also shows this asymmetry. The asymmetry is more likely to be due to many-body effects or well width variations. We intend to systematically study NIA and its effect on ISB splitting, if any. In order to eliminate well-to-well variations and band bending, we will grow only one well per sample, with a thick top AlSb barrier and an InAs cap layer, without doping. To explore the effects of NIA, we will vary the well width and interface layer thickness.

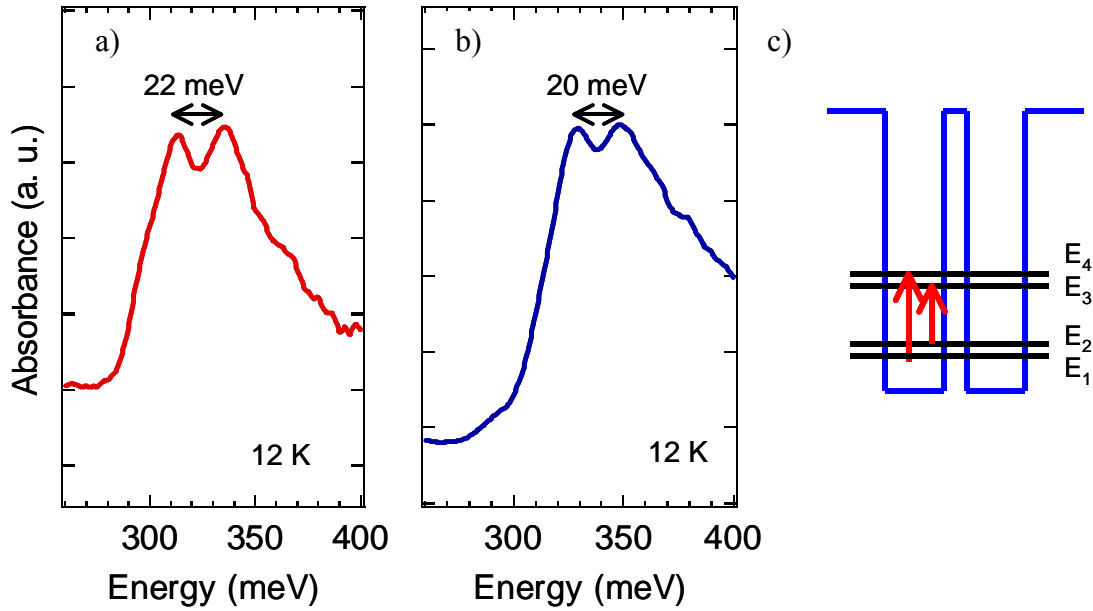


Figure 18: Intersubband absorption spectra of coupled double quantum wells with (a) 1.2 and (b) 1.5 nm central AlSb barriers (samples O and P). (c) shows the energy levels and transitions involved.

3.8 Coupled Double Quantum Wells

3.8.1 Symmetric

Figure 18 shows the intersubband absorption spectra of coupled double quantum wells with central AlSb barrier widths of 1.2 and 1.5 nm at 5 K (samples O and P). The absorption peak splittings are 22 meV and 20 meV, in agreement with calculations for E_1 - E_4 and E_2 - E_3 . The split peaks' amplitude decreases strongly with increasing temperature. In samples with narrower central AlSb barriers, we observe much weaker features which may be ISBA.

Figure 19: The calculated energy levels and wavefunctions for the asymmetric coupled double QW samples at 0 K, neglecting many-body interactions.

3.8.2 Asymmetric

Figure 19 shows the calculated energy levels and wavefunctions for the asymmetric coupled double QW structure at 0 K, neglecting many-body interactions. Figure 20 shows the intersubband absorption spectrum of one asymmetric coupled double quantum well (sample V). The sample is not intentionally doped and consists of 10 periods of InAs (14.4 nm) / AlSb (0.9 nm) / InAs (5.8nm), separated by 20 nm AlSb barriers. The total density is $1.4 \times 10^{13} \text{ cm}^{-2}$. At low temperature, this sample has two absorption peaks: a large one at 128 meV and a small one at 155 meV. At intermediate temperatures, a third peak appears as well around 142 meV. All three peaks persist to room temperature, as the middle peak gets more intense and the other two weaken. All of them redshift with

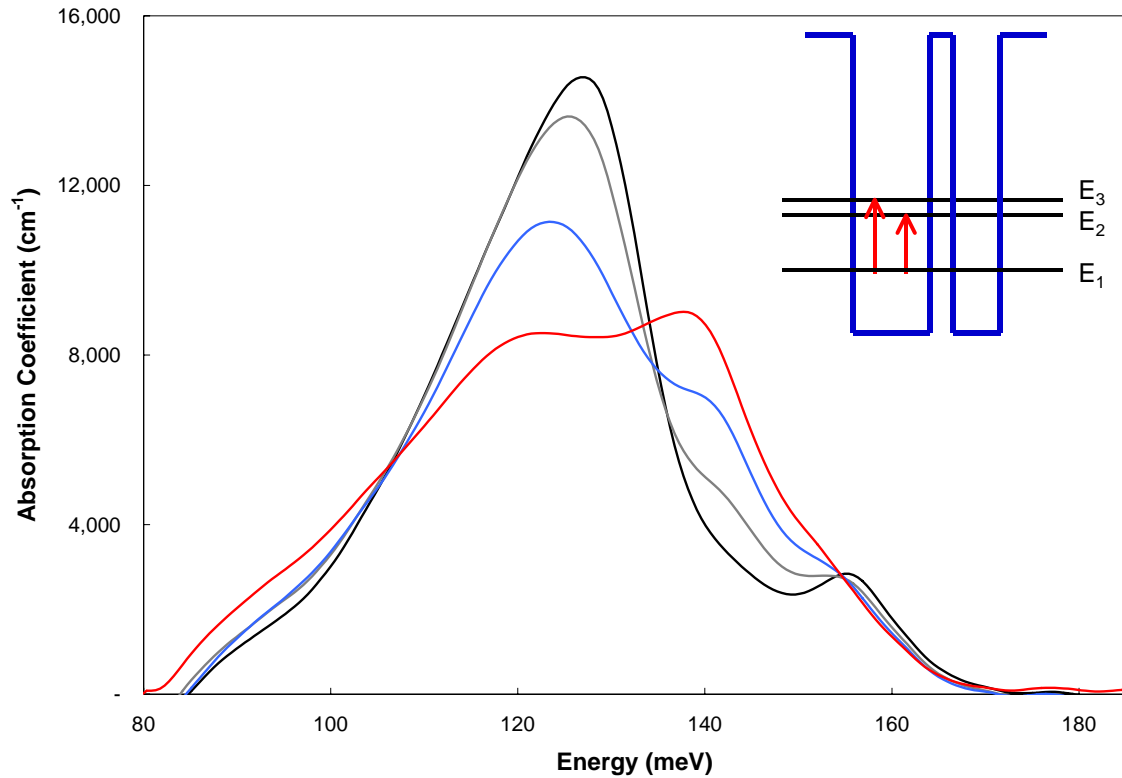


Figure 20: Intersubband absorption coefficient of undoped asymmetric coupled double QWs (sample V) at 12 K (black), 80 K (grey), 160 K (blue), and 300 K (red). The inset shows a cartoon of the energy levels in the heterostructure and the expected ISB transitions.

increasing temperature. We have also measured a sample with the same structure which is doped in the thicker well to $2.2 \times 10^{13} \text{ cm}^{-2}$ total density (sample U). This sample, shown in Fig. 21, has only one low temperature peak, at 126 meV. A shoulder around 142 meV appears at high temperature.

The peaks around 128 and 155 meV agree with envelope function calculations for E_{12} and E_{13} , shown in Fig. 19. The origin of the middle peak in sample V is unclear. It is too high energy to be E_{23} and too low to be a transition to level 4 or above. It may be due to spin-splitting of the subbands. For example, the middle peak may be a transition from the upper spin-split level of E_1 which may be populated only at higher temperatures. The final level of the transition could be either E_2 , which is consistent with the large amplitude of the middle peak, or E_3 , which is consistent with the energy of the peak. In

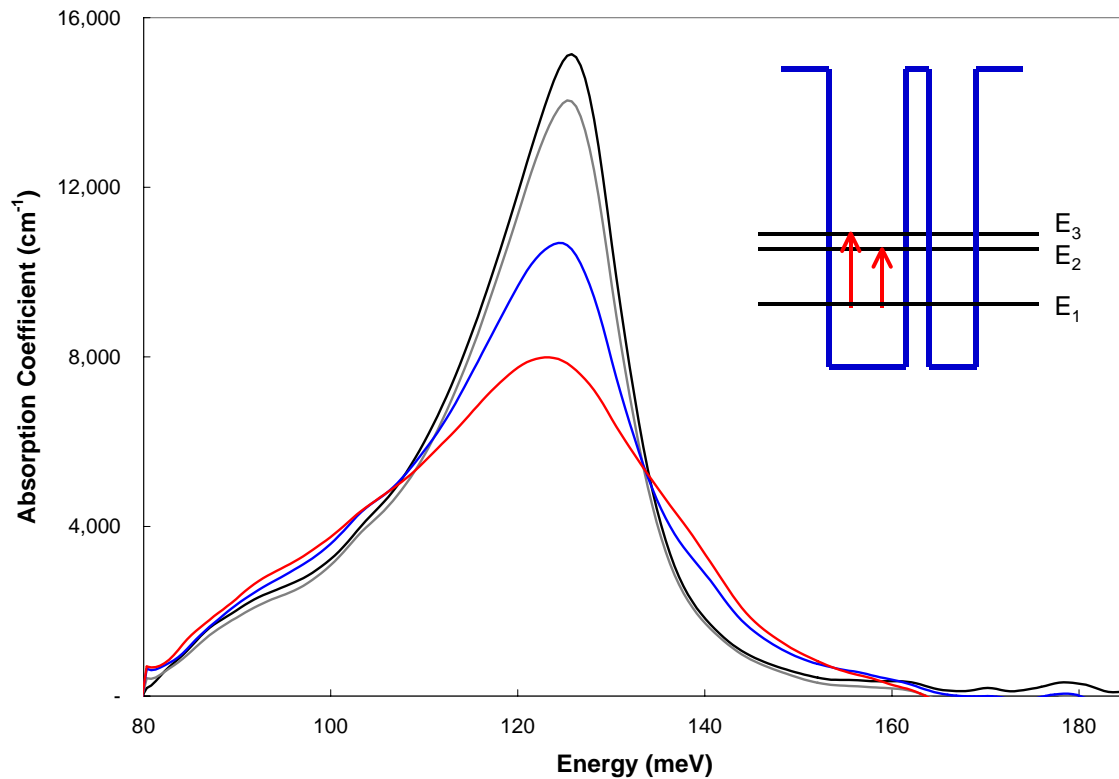


Figure 21: Intersubband absorption coefficient of doped asymmetric coupled double QWs (sample U) at 12 K (black), 80 K (grey), 200 K (blue), and 300 K (red). The inset shows a cartoon of the energy levels in the heterostructure and the expected ISB transitions.

sample U, the doping may alter the band profile of the QW enough to reduce the coherent interaction between the coupled well, eliminating the E_{13} peak.

3.9 Experimental conundrums

3.9.1 GaSb substrate

There are several unresolved questions about our spectra. The most distressing is the inability to observe ISBA in QWs grown on GaSb substrates. Although these substrates have a significant p -type free carrier density which causes some absorption in the spectral range of interest, the sample transmission is still large enough to permit easy observation of the ISBA. Perhaps the nature of the substrate changes the electron donor mechanism and the samples are not populated.

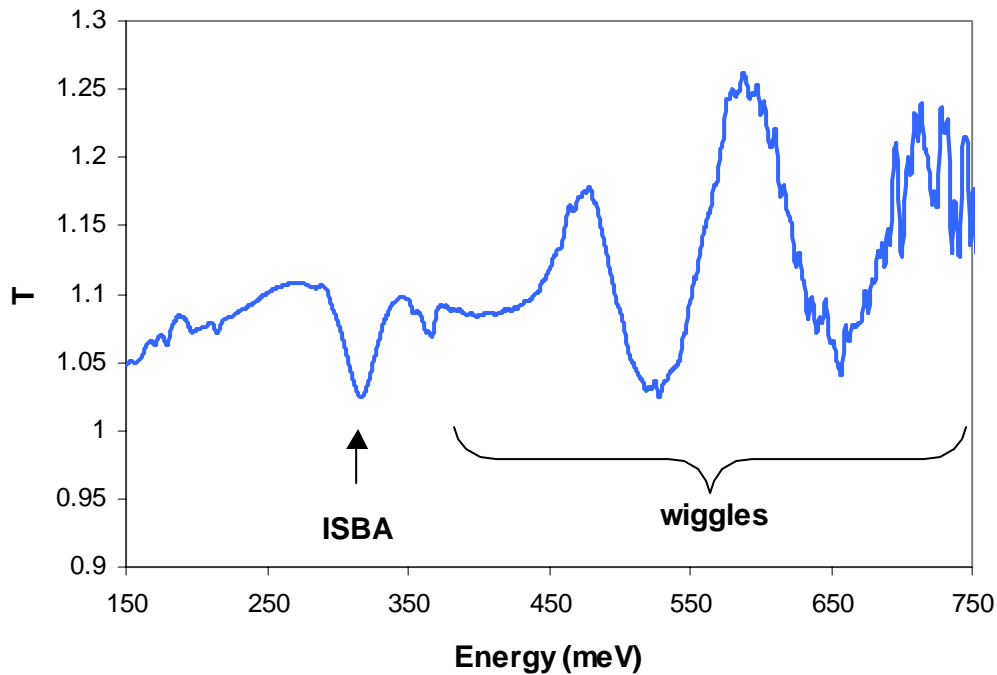


Figure 22: Typical T spectrum (sample W) showing sinusoidal wiggles and offset from $T = 1$.

3.9.2 Wiggles

Another question is the origin of large-period sinusoidal wiggles in the baseline of the T spectra, shown in Fig. 22. These wiggles have a period of 100-140 meV with an amplitude of up to 20% of T . They are present in most but not all samples; they are not present in GaSb-substrate samples. The positions of the wiggles occasionally match in samples which were grown sequentially and have similar densities.

What is the origin of these wiggles? At first glance, they look like Fabry-Perot interference fringes due to multiple reflections in a film. The film thickness that would give rise to these fringes is $1.3\text{-}0.9\ \mu\text{m}$ [using $\text{fringe period} = \sin(\theta) / 2n \text{ thickness}$], where n is the refractive index]. There are several combinations of layers in the sample that fit into this range of thicknesses, but there is nothing to provide the thickness variation of

400 nm over different samples. In addition, the wiggles occur in T spectra, so in fact they would indicate a *difference* in the multiple reflection of s - and p -polarized light.

3.9.3 Unexpectedly large absorption

In several high-density samples, T is less than 50% at the resonance. This unexpectedly large absorption seems to indicate that more than half of the p -polarized light is being absorbed. That is, some light polarized in the plane of the sample is being absorbed. But, a higher fraction of the in-plane light must be absorbed from the p beam than from the s . We cannot explain this result. This phenomenon has been observed elsewhere but without explanation.

3.9.4 Non-zero baseline

The origin of the addend R in the expression for the absorption coefficient is unclear. Mathematically, it means that T is not equal to 1 away from the resonance (Fig. 22). Physically, it indicates that there is polarization-dependent absorption at energies other than the resonance. One possible source of R is drift in the intensity ratio p/s over the course of the measurements, typically several hours for detailed temperature-dependent studies. However, T is typically greater than one even when the component spectra are taken in quick succession. Another possible reason that T is not one is that the reflectivities of the sides of the sample are different for different polarizations. In this case, s should be reflected more strongly than p , leading to $T < 1$, which is not what we observe.

3.10 Summary

In summary, we have observed interband and intersubband absorption in InAs/AlSb QWs. The absorption energy redshifts with increasing temperature, and the redshift is more pronounced for narrower wells. The distribution of electrons in the quantum wells strongly affects the ISBA. We have shown that a high electron density causes significant broadening, and that replacing the GaSb cap layer with InAs reduces band bending. We also expect that the linewidth of the ISBA will be reduced in a sample with a single well or with a thick top AlSb barrier, but our results are inconclusive. We have observed ISBA in doped QWs but not systematically studied the effects of doping. We have observed ISBA energies as high as 535 meV and expect to go higher. We plan to study the Rashba effect due to interface inversion asymmetry. We have observed the expected splitting of the ISBA in symmetric coupled double QWs. In asymmetric coupled double QWs for difference frequency generation, we have observed an unexpected third peak which grows with increasing temperature. Unresolved experimental issues include the inability to observe ISBA in QWs on GaSb substrates, a wiggly spectral baseline which is not centered around zero, and unexpectedly large ISBAs.

4 Theoretical Modeling

4.1 *k*·*p* model

4.1.1 Bulk dispersion relations

The ISBAs are modeled in two steps. First, the heterostructure dispersion relations and envelope wavefunctions are calculated in the ***k*·*p*** approximation. Then, the interaction of the system with light is calculated using the semiconductor Bloch equations, including many-body effects. The result of the calculation is the absorption coefficient of the ISBA.

The ***k*·*p*** model^{58,59} is a method for finding the dispersion relations of the bands in a crystal, that is, energy as a function of wavevector (***k***). It is valid only for ***k*** near a particular value of interest. First, we will consider the ***k*·*p*** model in bulk semiconductors, and then its extension to heterostructures is straightforward.

In order to find the dispersion relation, we solve the single particle Schrödinger equation $\left(\frac{p^2}{2m} + V(\mathbf{r})\right)\psi = E\psi$ using the Bloch function $\psi = Au_{n\mathbf{k}}e^{i\mathbf{k}\cdot\mathbf{r}}$ as a trial

wavefunction. Here $u_{n\mathbf{k}}$ is a crystal cell periodic part of the Bloch wavefunction of the electrons, $e^{i\mathbf{k}\cdot\mathbf{r}}$ is an extended part of the Bloch wavefunction, and n is the band index.

The form of the cell periodic part of the Bloch function depends on the band and the wavevector. This simplifies to the single electron Schrodinger equation in a bulk crystal⁶⁰:

$$\left(\frac{p^2}{2m} + \frac{\hbar \mathbf{k} \cdot \mathbf{p}}{m} + \frac{\hbar^2 k^2}{2m} + V \right) u_{n\mathbf{k}} = E_{n\mathbf{k}} u_{n\mathbf{k}}$$

$$(H + W(\mathbf{k})) u_{n\mathbf{k}} = E_{n\mathbf{k}} u_{n\mathbf{k}}$$

(Here we have neglected a k -dependent spin-orbit coupling term, which is included in the ISBA calculation.) At $\mathbf{k} = 0$, the \mathbf{k} -dependent terms drop out and the Schrödinger equation can be solved exactly to give a complete, orthonormal set of basis functions $u_{n,0}$. These are the band edge ($\mathbf{k} = 0$) Bloch functions, sometimes denoted

$$|S \uparrow\rangle, |X \uparrow\rangle, |Y \uparrow\rangle, |Z \uparrow\rangle, |S \downarrow\rangle, |X \downarrow\rangle, |Y \downarrow\rangle, |Z \downarrow\rangle$$

where the letter describes the atomic orbital-like symmetry of the bands and the arrow indicates the spin for the conduction band, heavy hole, light hole, and split off bands.

Now $E_{n,0}$ and $u_{n,0}$ can be used to calculate $E_{n,k}$, the dispersion relation, by treating the $\mathbf{k} \cdot \mathbf{p}$ and k^2 terms in the Hamiltonian as a perturbation. According to non-degenerate perturbation theory,

$$E_{n\mathbf{k}} = E_{n0} + \frac{\hbar^2 k^2}{2m} + \frac{\hbar^2}{m^2} \sum_{n' \neq n} \frac{|\langle u_{n0} | \mathbf{k} \cdot \mathbf{p} | u_{n'0} \rangle|^2}{E_{n0} - E_{n'0}} = E_{n0} + \frac{\hbar^2 k^2}{2m^*}$$

where $\frac{1}{m^*} = \frac{1}{m} + \frac{2}{m^2 k^2} \sum_{n' \neq n} \frac{|\langle u_{n0} | \mathbf{k} \cdot \mathbf{p} | u_{n'0} \rangle|^2}{E_{n0} - E_{n'0}}$

The dispersion relation is determined by m^* , the effective mass of the electron. The effective mass is different from the free electron mass due to coupling between electronic states in different bands, incorporated via the $\mathbf{k} \cdot \mathbf{p}$ term. Note that bands with a smaller energy difference between them have a stronger effect on m^* ; this is why narrow band gap semiconductors such as InAs have a light effective mass. Furthermore, the dispersion relation is nonparabolic, i.e. the effective mass is a function of wavevector or

energy. Nonparabolicity is stronger in narrow band gap semiconductors because of the larger $\mathbf{k}\cdot\mathbf{p}$ matrix element between nearby bands.

To get a simple expression for the conduction band effective mass, consider coupling only between the CB and the three near bands, HH, LH, and SO, because these have the largest contribution to the effective mass. Then:

$$\frac{1}{m^*_{CB}} \cong \frac{1}{m} + \frac{2|\langle S|\mathbf{k}\cdot\mathbf{p}|X,Y,Z\rangle|^2}{m^2 E_g k^2}$$

$$P = \frac{-i}{m_0} \langle S|p_x|X\rangle = \frac{-i}{m_0} \langle S|p_y|Y\rangle = \frac{-i}{m_0} \langle S|p_z|Z\rangle$$

$$\frac{m}{m_{CB}} \cong 1 + \frac{2P^2}{mE_g}$$

P is the interband matrix element of the momentum operator, \mathbf{p} , between the s -like conduction band and the p -like valence band. Experimentally, P is determined by comparison between $\mathbf{k}\cdot\mathbf{p}$ calculations and experiments such as interband magneto-optical absorption, cyclotron resonance, and electron spin resonance (ESR). ESR, for example, yields an effective g -factor which is almost entirely dependent on the interaction between the conduction band and the nearby valence bands.⁶¹

One way to make a more precise calculation of the dispersion relation would be to include higher order corrections in the perturbation theory. A more popular method is the Kane model, which takes advantage of the fact that four of the bands (the conduction band, heavy hole, light hole, and split-off bands) are close together in energy and also far from all the other bands (Fig. 23). In this model, the Schrödinger equation is solved exactly for these four bands, then the effects of remote bands are included perturbatively.

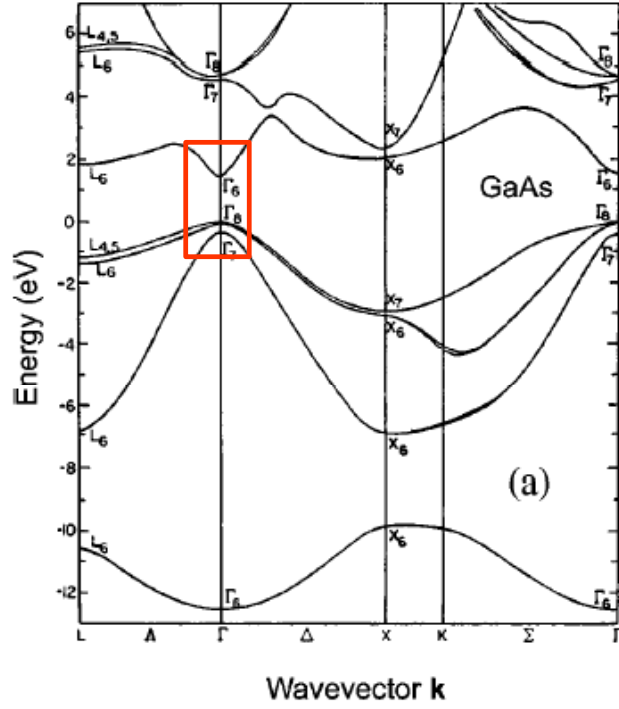


Figure 23: Band structure of GaAs, with the near-gap bands at the Γ point highlighted in red.

We solve the Schrödinger equation in a basis set in which spin-orbit coupling is already diagonal. The Bloch functions that make up this basis set are:

$$\begin{aligned}
 \text{CB: } & \left| \frac{1}{2}, \pm \frac{1}{2} \right\rangle = i |S \uparrow\rangle, i |S \downarrow\rangle \\
 \text{HH: } & \begin{cases} \left| \frac{3}{2}, \frac{3}{2} \right\rangle = \frac{1}{\sqrt{2}} |(X+iY) \uparrow\rangle \\ \left| \frac{3}{2}, -\frac{3}{2} \right\rangle = \frac{1}{\sqrt{2}} |(X-iY) \downarrow\rangle \end{cases} \\
 \text{LH: } & \begin{cases} \left| \frac{3}{2}, \frac{1}{2} \right\rangle = -\sqrt{\frac{2}{3}} |Z \uparrow\rangle + \frac{1}{\sqrt{6}} |(X+iY) \downarrow\rangle \\ \left| \frac{3}{2}, -\frac{1}{2} \right\rangle = -\sqrt{\frac{2}{3}} |Z \downarrow\rangle - \frac{1}{\sqrt{6}} |(X-iY) \uparrow\rangle \end{cases} \\
 \text{SO: } & \begin{cases} \left| \frac{1}{2}, \frac{1}{2} \right\rangle = \sqrt{\frac{1}{3}} |Z \uparrow\rangle + \frac{1}{\sqrt{3}} |(X+iY) \downarrow\rangle \\ \left| \frac{1}{2}, -\frac{1}{2} \right\rangle = \sqrt{\frac{1}{3}} |Z \downarrow\rangle - \frac{1}{\sqrt{3}} |(X-iY) \uparrow\rangle \end{cases}
 \end{aligned}$$

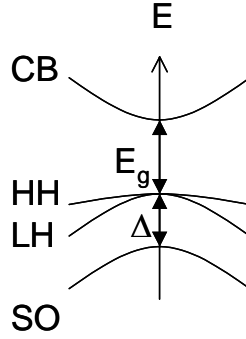


Figure 24: Bands and energy separations.

The good quantum numbers are the total angular momentum, J , and its projection along the z axis, m_J . Group theory describes how the basis set transforms under various symmetry operations, which allows us to find the matrix elements of W . The eigenvalues of $W(\mathbf{k})$ are the energies of the bands as a function of wavevector. The parameters in the W matrix are P , E_g the band gap, and Δ , the spin-orbit coupling energy. Also included in the Kane model are interactions with remote bands and the lack of inversion asymmetry in zincblende crystals (e.g. III-V semiconductors), which leads to anisotropy. Now the effective mass of the lowest conduction band is:

$$\frac{1}{m_{CB}} = \frac{1}{m_0} + \frac{4P^2}{3E_g} + \frac{2P^2}{3(E_g + \Delta)}$$

$$\frac{m_{CB}(\lambda)}{m_{CB}(0)} = \frac{(\lambda + E_g)(\lambda + E_g + \Delta)(E_g + 2\Delta/3)}{E_g(E_g + \Delta)(\lambda + E_g + 2\Delta/3)}$$

$$\text{where } \lambda(k) = E(k) - \frac{\hbar^2 k^2}{2m_0}$$

So, how good is the $\mathbf{k}\cdot\mathbf{p}$ model compared to more exact calculations of the band structure such as the tight binding model? The $\mathbf{k}\cdot\mathbf{p}$ model no longer matches the tight binding calculation when one of the “remote bands” gets close in energy to the bands of

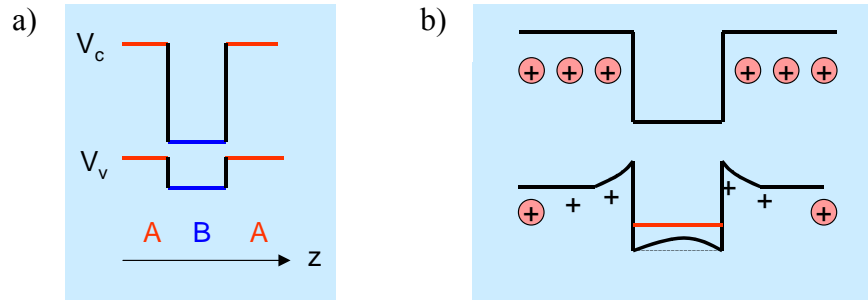


Figure 25: (a) Band edge profile of a heterostructure. (b) CB profile of a heterostructure without and with self-consistent charge transfer.

interest. For the CB in GaAs, this happens at an energy of about 0.3 eV above the band edge--good enough for describing heterostructures. $\mathbf{k}\cdot\mathbf{p}$ calculations are also much more accurate than tight-binding methods near the band edge.

4.1.2 Heterostructure: Envelope Function description

To apply the $\mathbf{k}\cdot\mathbf{p}$ model to heterostructures, we use the envelope function description. Here, the wavefunction in each layer is the periodic part of the Bloch function times F , which is the envelope of the wavefunction on the scale of the heterostructures.

$$\Psi(\mathbf{r}) = \begin{cases} \sum_n F_n^A(\mathbf{r}) u_{n,\mathbf{k}}^A(\mathbf{r}) \\ \sum_n F_n^B(\mathbf{r}) u_{n,\mathbf{k}}^B(\mathbf{r}) \end{cases}$$

The core assumption of the envelope function description is that the cell periodic parts of the Bloch functions in the different materials are the same.

The Schrödinger equation for the envelope functions is like that in the bulk case, except \mathbf{k} is replaced by the velocity operator and the band edge potentials depend on the position in the heterostructure [Fig. 25(a)]. Then, solving for the envelope functions is a lot like solving for a one-dimensional potential in elementary quantum mechanics. This is why the envelope function approximation is so easy, popular, and powerful. The

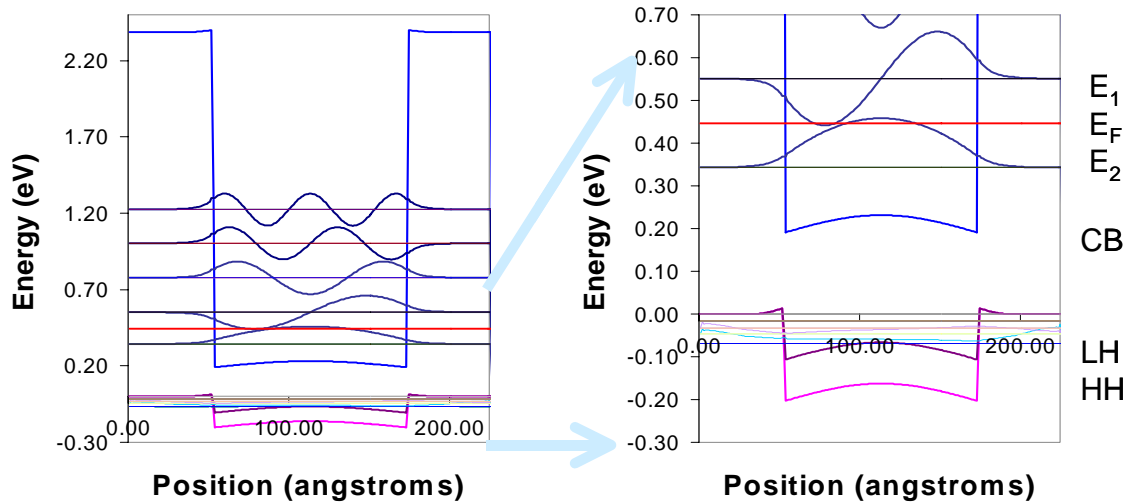


Figure 26: Calculated low-energy envelope functions for an InAs/AlSb QW. The expanded figure shows the near-gap levels.

Hamiltonian also contains a slowly-varying external potential due to self-consistent charge transfer in modulation-doped heterostructures [the Hartree term; Fig. 25(b)] and some other terms due to strain.

The boundary conditions on the envelope function are that it must be continuous at the interfaces, and its derivative times a complicated function of the effective masses in the two materials must also be continuous.

Figure 26 shows the calculated envelope functions for an InAs/AlSb QW. The well is 10 nm wide, and the electron density is $1.84 \times 10^{12} \text{ cm}^{-2}$. The red line is the Fermi level, so at this density, only the lowest subband is populated. The bottom of the well is bent up by 40 meV due to charge transfer. The light hole band is 100 meV above the heavy hole band due to biaxial tensile strain in the InAs, which also decreases E_g .

Figure 27 shows the calculated dispersion relations for the well in Fig. 26. The red line is the Fermi level and the blue lines are the conduction band levels. Overlaid on Fig. 27 is a parabolic energy level. By comparing this with the real, non-parabolic level,

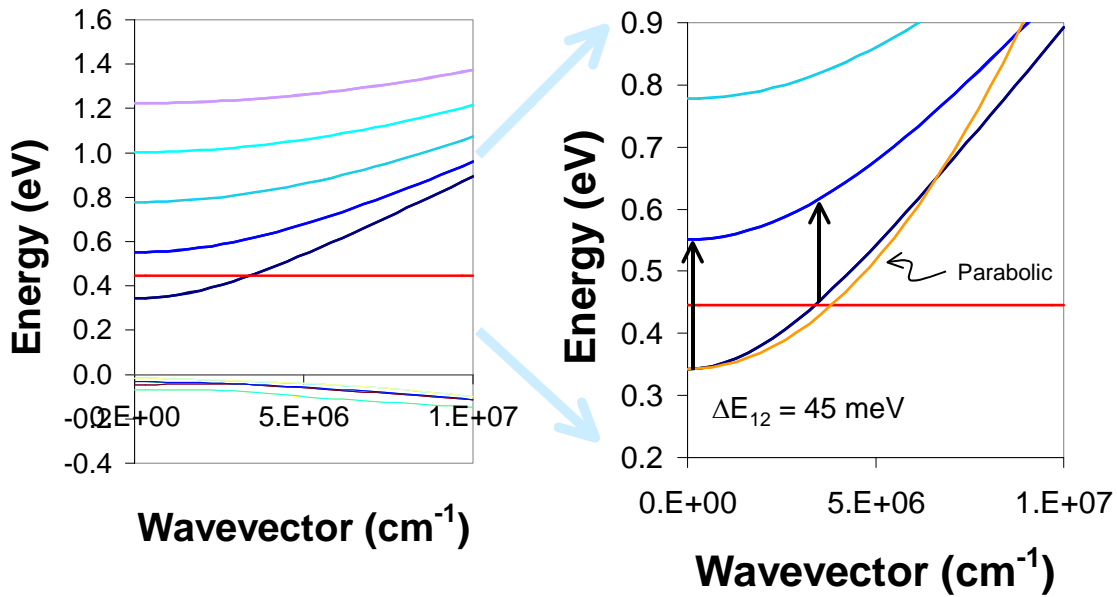


Figure 27: Dispersion relation for the QW in Fig. 24. The red line is the Fermi energy at 0 K. A parabolic dispersion is included in orange to demonstrate the nonparabolicity of the actual dispersion.

it is clear that the effective mass of the nonparabolic level increases with increasing wavenumber.

The lowest level is more nonparabolic than the higher levels because it is closer in energy to the valence band. This change in the degree of nonparabolicity with energy level broadens the intersubband absorption because electrons at different wavevectors see different subband separations. For example, at 0 K, the subband separation is 208 meV at $\mathbf{k} = 0$ and 166 meV at the edge of the filled states, so the expected width of the intersubband absorption is $208 - 166 = 42$ meV. But in fact, the observed absorption is less than half as broad. The resonance behaves so differently from the single-particle calculation due to the strong effect of many-body interactions.

4.2 Absorption calculation

4.2.1 Intersubband Semiconductor Bloch Equations

Many-body interactions play a critical role in intersubband absorption. In order to incorporate them properly into the model, we have chosen to calculate the absorption coefficient using the semiconductor Bloch equations (SBEs)^{47,62} to describe the interaction of a semiconductor with light.

The SBEs⁶³ describe the interaction of a semiconductor with light through the dipole interaction. They provide the most general formalism to incorporate coherent and incoherent light-semiconductor interactions by taking into account band dispersions, Coulomb interactions, and various decoherence and relaxation processes. They are an extension of the Bloch equations (which is for describing the dynamics of a magnetic moment in a time-dependent magnetic field) and the optical Bloch equations (which is for describing the dynamics of a two-level atom in a laser field). The SBEs have been successfully applied to the study of interband dynamics in many semiconductor systems, but this is one of the first cases where they are applied to intersubband dynamics.

Important parameters in the Bloch equations are T_1 , the population relaxation time, T_2 , the spin relaxation time, and Ω_R , the Rabi frequency, which is related to the moment's oscillation frequency. We use the reduced single particle density matrix:

$$\begin{pmatrix} \langle a_k^+ a_k \rangle & \langle b_{-k} a_k \rangle \\ \langle a_k^+ b_{-k}^+ \rangle & \langle b_k^+ b_k \rangle \end{pmatrix} = \begin{pmatrix} n_k^c & P_k \\ P_k^* & n_k^v \end{pmatrix}$$

where (a^+, a) and (b^+, b) are the electron and hole creation and annihilation operators, respectively, P_k is the electron-hole transition amplitude, and $n_k^{c,v}$ are the conduction and

valence band occupation probabilities. The Hamiltonian contains a single-particle energy, Coulomb interaction between carriers, and dipole interaction between carriers and light. We use the Heisenberg equation of motion to derive the coupled equations of motion for P_k and $f_k^{c,v}$. The resulting Hartree-Fock interband semiconductor Bloch equations are:

$$\begin{cases} \frac{\partial P_{\mathbf{k}}}{\partial t} = -i(e_{e_2,\mathbf{k}} + e_{e_1,\mathbf{k}})P_{\mathbf{k}} - i(n_{e_2,\mathbf{k}} + n_{e_1,\mathbf{k}} - 1)\varpi_{R,\mathbf{k}} + \frac{\partial P_{\mathbf{k}}}{\partial t}\Big|_{coll} \\ \frac{\partial n_{e_2,\mathbf{k}}}{\partial t} = -2\text{Im}(\varpi_{R,\mathbf{k}}P_{\mathbf{k}}^*) + \frac{\partial n_{e_2,\mathbf{k}}}{\partial t}\Big|_{coll} \\ \frac{\partial n_{e_1,\mathbf{k}}}{\partial t} = -2\text{Im}(\varpi_{R,\mathbf{k}}P_{\mathbf{k}}^*) + \frac{\partial n_{e_1,\mathbf{k}}}{\partial t}\Big|_{coll} \end{cases}$$

$$\begin{aligned} \hbar e_{e_2,\mathbf{k}} &= \hbar E_{e_2,\mathbf{k}} - \sum_{\mathbf{q}} V_{|\mathbf{k}-\mathbf{q}|} n_{e_2,\mathbf{q}} \\ \varpi_{R,\mathbf{k}} &= \frac{1}{\hbar} \left[d_{21}\mathcal{E} + \sum_{\mathbf{q} \neq \mathbf{k}} V_{|\mathbf{k}-\mathbf{q}|} P_{\mathbf{q}} \right] \end{aligned}$$

In these equations, d is the dipole matrix element between final and initial states. e is the renormalized single-particle energy, equal to the single-particle energy plus the exchange self-energy (a many-body effect described later). ω_R is the generalized Rabi frequency. It describes the fact that the system reacts to an effective field that is the sum of the applied field and the dipole field of all the excited electron-hole pairs. The $\text{Im}(\omega_{R,\mathbf{k}}P_{\mathbf{k}}^*)$ terms describe the generation of electrons and holes by light. The collision term on the polarization represents dephasing, like T_1 , and the collision terms on the population represent decay, like T_2 . The SBEs also include phase space filling. The SBEs apply to light intensities which are strong enough to create enough excited electrons that there is significant Coulomb interaction between carriers. If there were no Coulomb interaction, which would happen if the excitation intensity were very low, then V would go to zero and the generalized Rabi frequency would be the usual Rabi frequency.

For intersubband semiconductor Bloch equations, the electron and hole levels are replaced by two lowest CB energy levels. In this case the dispersion relation of the lower level now has the same curvature direction as the upper level, rather than opposite as in the interband case. The semiconductor Bloch equations are usually applied to interband phenomena; this is one of their first applications to intersubband resonances.⁶⁴

4.2.2 Many-body Effects

The four types of Coulomb interaction can be classified according to whether they are direct or exchange, and static or dynamic. We have already discussed the direct, static Coulomb interaction. This causes band bending and screening and is included in the band structure calculation via the heterostructure potential, according to the Hartree approximation. The exchange, static Coulomb interaction is the self-energy correction.⁶⁵ This correction arises because, in the Hartree approximation, the wavefunction does not satisfy the Pauli principle. When the wavefunction is made antisymmetric under particle exchange, it gains the self-energy, also known as the Fock term.

The direct, dynamic Coulomb interaction is known as the depolarization shift, or resonant screening. Allen *et al.*⁶⁶ showed that the ISBA could not be described by static many-body effects alone. They found that they had to take into account the screening of the applied electric field by the carriers, which causes the effective field to be smaller than the applied field. So, the absorption occurs at a higher applied frequency. The depolarization shift is larger for larger densities. Calculating the size of the shift requires calculating the frequency dependence of the polarization.

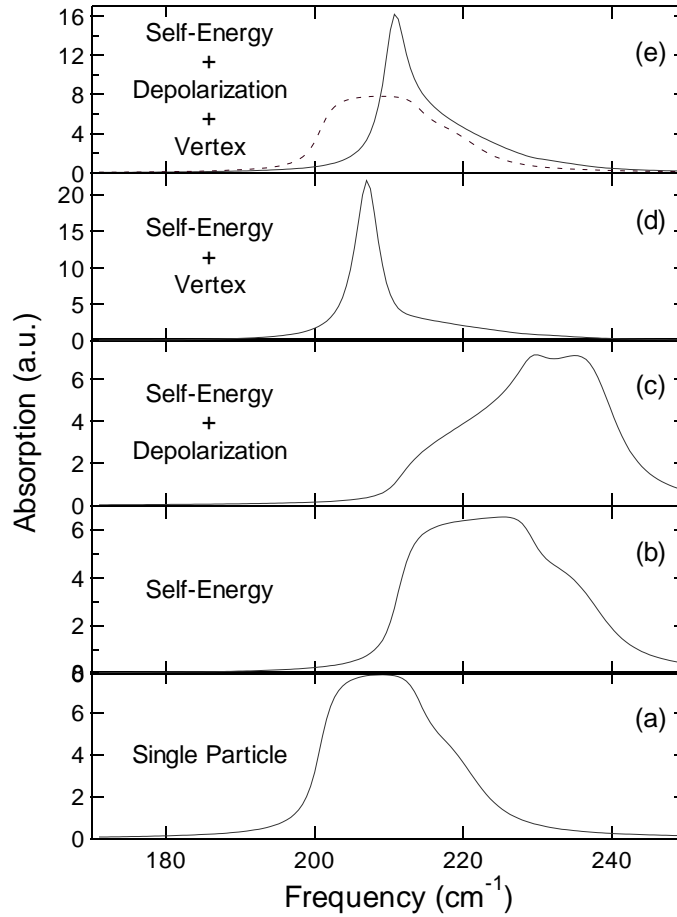


Figure 28: Calculated ISBA spectra for 10 nm InAs/AlSb QW at 4.5 K with a density of $8 \times 10^{11} \text{ cm}^{-2}$. The effects of many-body interactions on the intersubband absorption are shown singly and in combination. In (e), the dotted line is the single particle spectrum.

The exchange, dynamic Coulomb interaction is the excitonic or vertex correction. It is the interaction between an excited electron and the remaining electrons. Ando showed that it partially cancels the depolarization shift.⁶⁷ Figure 28 shows the effects of the many-body interactions one at a time. Figure 28(a) is the single-particle spectrum, which is broad due to nonparabolicity. Adding the self energy shifts the resonance to higher energy and broadens it slightly, as does the depolarization shift. The vertex correction causes a strong redshift and a dramatic narrowing of the resonance. The vertex correction turns out to be the dominant effect in this regime. However, the

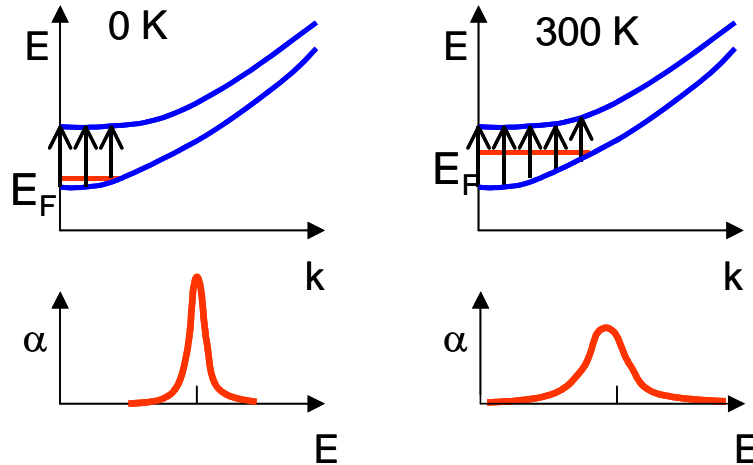


Figure 29: Nonparabolic dispersion relation and absorption coefficient at 0 K and 300 K. The arrows indicate the single-particle ISBA energies.

interplay of many-body effects is sensitive to carrier density and well width. In general, for a fixed density, the vertex correction is more important in narrower wells and the depolarization effect is more important in wider wells.

4.2.3 Temperature dependence

The temperature dependence of the ISBA is incorporated through the carrier density, band filling, and nonparabolicity. The temperature dependence of phonon scattering is not included. This simple treatment reproduces the experimental energy shift and linewidth change well. At low temperatures, the carrier density is low and the carriers are all at the lowest possible energies [Fig. 29(a)]. This gives the minimum nonparabolicity broadening and a sharp absorption line. At room temperature, the carrier density is about three times higher and the carriers are thermally excited to higher energies in the subband [Fig. 29 (b)]. This redistribution strongly increases the nonparabolicity broadening, shifting the resonance to lower energy and broadening it. Because GaAs has smaller nonparabolicity, ISBA in GaAs/AlGaAs QWs show smaller redshifts.^{44,45,46}

5 Conclusions

In conclusion, we have investigated intersubband absorption in InAs/AlSb QWs. We have observed ISBA energies as high as 535 meV in 3 nm QWs. We have observed a strong redshift of the ISBA energy with increasing temperature, which we have modeled via band filling and nonparabolicity. We have investigated the charge distribution in our samples and its effect on the ISBA, and we have improved the distribution. We have observed ISBA in coupled double quantum well structures, notably in an asymmetric structure which is suitable for ISB THz difference frequency generation. We have developed a model based on the intersubband semiconductor Bloch equations which incorporates the major many body effects to successfully describe the lineshape of the ISBAs.

In the future, we will expand our experimental capabilities. We will detect ISBA in unpopulated narrow wells using electrical gating and interband pumping to provide carriers for modulation spectroscopy. We will explore THz difference frequency generation in asymmetric double quantum wells using mid-infrared quantum cascade lasers as intersubband pumps. We anticipate that this new THz source will find ready application amongst the growing arsenal of THz sources.

6 Appendix A: How-to

6.1 *Annealing In contacts for transport measurements*

In order to make a good contact, everything must be clean.

1. Cut a square sample, at least 3 mm x 3 mm.
2. Soak the sample in acetone for at least an hour. Remove and dry with compressed air.
3. Put a tiny blob of indium on each corner of the sample. The indium must be clean and not oxidized, so cut off the dull oxidized part of the indium with a razor before cutting off some for contacts. You need to have a microscope to see what you're doing, 3-5 X magnification with a large field of view. Here are two ways to put blobs on:
 - a. With a solder iron. You have to have a steady hand for this. Use the solder iron and tip for indium only, not for ordinary solder. Put the indium on a clean glass slide. Use the lowest temperature possible. Indium melts at 160 °C.
 - b. Cut a tiny blob of indium and smush it onto the sample using the corner of a glass slide (cleaned with acetone, of course).

The indium should be as close to the corners as possible but not touch the sides. If it gets on the sides, it might short with the sample holder.

4. Anneal the contacts.
 - a. Put the sample into the annealing box.

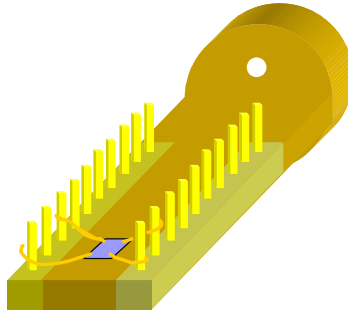


Figure 30: Transport sample holder with sample attached. From S. M. Crankshaw, “Characterization of Antimonide-Based Compound Semiconductors and Quantum Wire Fabrication,” B. S. thesis, Rice University, April 2003.

- b. Run several L/min of annealing gas through the box for a few minutes.

The gas should be **80% dry N₂, 20% He or H₂**. The purpose of the annealing gas is to prevent oxidation of the sample and contacts. A gas mixture with H₂ requires a different kind of regulator connector than mixtures with only N₂ or He.
 - c. Turn on the current and heat up the sample to **230 °C**. Leave it at that temperature for 1-10 minutes, and then turn off the current.
 - d. Leave the gas running for 5 minutes while the sample cools down.
5. Connect wires to the contacts. The wires should be gold, ~0.002” dia., from e.g. California Fine Wire Co. Cut four wires 2 cm long with a razor blade. Again, there are two ways:
- a. With a solder iron. Get a little bit more indium and use it to glue the tip of the wire to the contact.
 - b. Make an indentation in the contact with a razor blade. Lay the wire in the indentation and then use a glass slide to smush a tiny piece of indium on top of it. After gluing on all four wires, put the sample on a glass slide on a hotplate. Watch for the indium to melt and take it off immediately.

6. Glue the sample to the sample holder with rubber cement. Connect the wires to the pins on the holder with solder, as shown in Fig. 30.

6.1.1 How to make your own annealing box

Make a small, $\sim 1 \text{ ft}^3$ box out of plexiglass. Make some holes for the annealing gas to come in (via a flow meter) and go out. To heat the sample, use a large AC current, i.e. a very low voltage. Connect a variable transformer to the wall plug, and then connect that to the biggest transformer you can find. Use thick wires to carry the high current, and connect them across a $0.5 \times 3 \text{ cm}$ sheet of chromium. This is the part that will get hot. Put it inside the box. Use a thermocouple for the temperature sensor. Weld it to the underside of the chromium. When you anneal, put the sample right over the thermocouple.

6.2 Electrical set-up for SdH/Hall measurements

To apply the current, source 2 V from a lock-in at 17 Hz (quasi-DC). Apply this across the sample in series with a $2 \text{ M}\Omega$ and a $1 \text{ k}\Omega$ resistor outside the magnet for $\sim 1 \mu\text{A}$ of current. Read the voltage across the other pair of contacts. Typical resistances across the sample are in the 10's of ohms at room temperature and low temperature. To check the current, read the voltage across the $1 \text{ k}\Omega$ resistor.

6.3 Gold coating for ISBA measurements

Use a thermal evaporator. Pump it to 3×10^{-6} torr (not as low as for nanoscopic electronic devices). Evaporate 20 \AA of Cr at $0.5 \text{ \AA}/\text{min}$. Then evaporate 980 \AA of Au at

2-3 Å /min. Source for evaporation supplies: R. D. Mathis Co. Chromium rod: CRW-1.
Tungsten boat for holding gold pellets: ME21 0.005W.

6.4 Polishing for ISBA measurements

We have a hand polisher from South Bay Technologies (model 150), plus sample pucks at several angles, mounting wax (135), and a lot of different sizes of grit. To polish:

1. Wipe off the puck with acetone.
2. Heat up the puck on a hotplate and melt some wax on it.
3. Put the sample on the puck using metal tweezers. If you are polishing it at an angle, the sample must stick out beyond the top of the puck. Leave more of it sticking out than you actually want to remove. Cover the sample with a thin layer of wax to prevent the grit from damaging it.
4. Put the puck on a piece of metal to cool quickly.
5. Mount the puck in the polisher
6. Put about 1 ½ teaspoons of grit onto a piece of glass ~6" in diameter. Put some water on it, enough for the polisher to move easily. Rub the polisher around in the grit until you have removed what you want.
7. Rinse off the polisher and glass, then repeat with the next grit.
8. Remove the sample from the puck by melting the wax. Clean the sample in acetone.

To make parallelogram samples for ISBA measurements, start with a rectangular piece 3-3.5 mm wide and as long as possible, up to ~1 cm. Coat the QW side with gold before polishing.

If you want to polish the substrate side, do this first. You don't have to cover the substrate with wax, but do cover the edges. I tried making the substrate shiny but it didn't seem to improve the transmission through the sample. If you want to make two samples exactly the same thickness, put them on the same puck and leave them on the hotplate for 5 minutes so the wax gets very runny underneath.

To make parallelogram samples, polish the two long edges at 45°. I like to wind up with the gold side out on the second edge so that it's easier to make sure the edge that's already polished is parallel with the edge of the puck. You can also use a magnifier to check this. Make sure that more of your sample is sticking off the edge of the puck than you actually want to polish.

Polishing recipe:

1. 10.5 μm grit. This takes off a lot of material so check your sample every 10-20 strokes. For 45° edge, polish until you've just started to take off the edge of the sample. If you just want to make your GaAs flat, not shiny, this is the only grit you need.
2. 5 μm grit: skip this one: it's too sticky.
3. 3 μm grit: for the 45° edge, polish until it's just barely all 45°.
4. 0.9 μm grit: at least 5 minutes.
5. 0.5 μm grit: at least 5 minutes.

The longer you polish with the smallest grits, the shinier your sample will be.

7 Appendix B: Samples

See chart on the following pages.

name	period	sample number	sub.	InAs thickness	QW period	interface2 (on InAs)	interface1 (on AlSb)	doping
A	33	0111121T-M	GaAs	10.0	20	InSb(3.6s)	InSb(3.6s)	
	34	0111122T-M	GaAs	6.0	20	InSb(3.6s)	InSb(3.6s)	
	19	0112201T-M	GaAs	2.4	20	InSb(3.6s)	InSb(3.6s)	
	20	0112202T-M	GaAs	2.7	20	InSb(3.6s)	InSb(3.6s)	
B	25	0201181T-M	GaAs	7.4	20	InSb(3.6s)	InSb(3.6s)	
C	26	0201182T-M	GaAs	8.4	20	InSb(3.6s)	InSb(3.6s)	
W	30	0201251T-M	GaAs	6.5	20	InSb(3.6s)	InSb(3.6s)	
	31	0201252T-M	GaAs	3.7	20	InSb(3.6s)	InSb(3.6s)	
	13	0203062T-M	GaAs	5.6	20	InSb(3.6s)	InSb(3.6s)	
D	5	0205171T-M	GaAs	10.5	20	AlAs(3.6s)	InSb(3.6s)	
	6	0205201T-M	GaAs	3.2	20	AlAs(3.6s)	InSb(3.6s)	
E	7	0205221T-M	GaAs	10.5	20	AlAs(3.6s)	InSb(3.6s)	Si
	8	0205241T-M	GaAs	3.2	20	AlAs(3.6s)	InSb(3.6s)	Si
	9	0205271T-M	GaAs	3.2	20	InSb(3.6s)	InSb(3.6s)	Si
	10	0205291T-W	GaSb	3.2	20	InSb(3.6s)	InSb(3.6s)	
	11	0206031T-W	GaSb	10.5	20	InSb(3.6s)	InSb(3.6s)	
	12	0206051T-M	GaAs	3.2	20	InSb(3.6s)	InSb(2.6s)	
	13	0206071T-M	GaAs	10.5	20	InSb(3.6s)	InSb(2.6s)	
	6	0207102T-W	GaSb	3.2	20	InSb(2.6s)	InSb(2.6s)	
	9	0207152T-W	GaSb	2.3	20	InSb(2.6s)	InSb(2.6s)	
	13	0207221T-W	GaSb	6.0	20	InSb(2.6s)	InSb(2.6s)	
	14	0207222T-M	GaAs	9.0	20	InSb(2.6s)	InSb(2.6s)	
	15	0207241T-W	GaSb	4.5	20	InSb(2.6s)	InSb(2.6s)	
	16	0207242T-M	GaAs	9.0	20	AlAs(3.6s)	InSb(2.6s)	
	19	0207291T-W	GaSb	3.2	20	AlAs(3.6s)	InSb(3.6s)	
	20	0207292T-M	GaAs	3.2	20	InSb(2.6s)	InSb(2.6s)	
	21	0207311T-W	GaSb	3.2	20	InSb(3.6s)	InSb(3.6s)	
	22	0207312T-M	GaAs	3.2	20	InSb(3.6s)	InSb(3.6s)	
	23	0208021T-W	GaSb	5.1	20	InSb(2.6s)	InSb(2.6s)	
	24	0208022T-M	GaAs	3.2	20	AlAs(3.6s)	InSb(2.6s)	
	25	0208061T-W	GaSb	3.2	20	AlAs(3.6s)	AlAs(3.6s)	
	27	0208081T-W	GaSb	3.2	20	no interface	no interface	
	29	0208211T-W	GaSb	3.2	20	InSb(3.6s)	InSb(2.6s)	
	30	0208212T-M	GaAs	3.2	20	InSb(3.6s)	InSb(3.6s)	
	33	0208271T-W	GaSb	6.5	20	InSb(2.6s)	InSb(2.6s)	
	34	0208272T-M	GaAs	3.2	20	InSb(3.6s)	InSb(2.6s)	
	35	0208291T-W	GaSb	3.2	20	InSb(2.6s)	InSb(1.6s)	
	36	0208292T-M	GaAs	5.5	20	InSb(2.6s)	InSb(2.6s)	
	37	0209021T-W	GaSb	3.2	20	InSb(2.6s)	InSb(3.6s)	
	38	0209022T-M	GaAs	7.0	20	InSb(2.6s)	InSb(2.6s)	
	39	0209041T-W	GaSb	10.0	20	InSb(3.6s)	InSb(3.6s)	
F	40	0209042T-M	GaAs	10.0	20	InSb(3.6s)	InSb(3.6s)	
	41	0209091T-M	GaAs	6.4	20	InSb(3.6s)	InSb(3.6s)	
G	43	0209111T-M	GaAs	10.0	20	InSb(3.6s)	InSb(3.6s)	
	6	0211011T-M	GaAs	2.7	20	InSb(3.6s)	InSb(3.6s)	

name	sample number	300K Hall		77K Hall		4.2 K Hall
		mobility (cm ² /Vs)	density (cm ⁻²)	mobility (cm ² /Vs)	density (cm ⁻²)	mobility (cm ² /Vs)
A	0111121T-M	9488	5.47E+12	29884	2.56E+12	55783
	0111122T-M	3279	4.19E+12	8005	1.81E+12	
	0112201T-M	246	3.49E+13	356	9.06E+12	
	0112202T-M	468	2.29E+13	181	2.34E+13	
B	0201181T-M	7694	1.83E+13	10908	1.68E+13	-
C	0201182T-M	9017	1.46E+13	14985	1.20E+13	11320
W	0201251T-M	4564	5.52E+12	8368	2.74E+12	-
	0201252T-M	685	7.31E+12	351	2.37E+12	
	0203062T-M	2784	4.44E+12	5654	1.86E+12	
D	0205171T-M	11385	8.33E+13	22178	8.31E+13	20990
	0205201T-M	1448	3.44E+13	1425	3.31E+13	
E	0205221T-M	9162	5.02E+13	14671	4.84E+13	
	0205241T-M	726	2.63E+13	426	2.80E+13	
	0205271T-M	1086	2.59E+13	746	2.63E+13	
	0205291T-W					
	0206031T-W					
	0206051T-M	1014	1.28E+13	391	1.79E+13	
	0206071T-M	8235	9.80E+12	17269	6.32E+12	
	0207102T-W					
	0207152T-W					
	0207221T-W					
	0207222T-M	8254	5.18E+12	33035	1.92E+12	
	0207241T-W					
	0207242T-M	5948	4.71E+12	21778	1.76E+12	
	0207291T-W					
	0207292T-M	236	2.15E+13	645	6.27E+12	
	0207311T-W					
	0207312T-M	169	3.14E+13	790	5.40E+12	
	0208021T-W					
	0208022T-M	331	2.23E+13	483	9.97E+12	
	0208061T-W					
	0208081T-W					
	0208211T-W					
	0208212T-M	177	2.23E+13	740	3.83E+12	
	0208271T-W					
	0208272T-M	69	6.59E+13	687	4.55E+12	
	0208291T-W					
	0208292T-M	2429	4.50E+12	7614	1.50E+12	
	0209021T-W					
	0209022T-M	4558	3.74E+12	17886	1.68E+12	-
	0209041T-W					
F	0209042T-M	11414	3.17E+12	75029	1.38E+12	118894
	0209091T-M	2066	4.07E+12	5317	1.52E+12	
G	0209111T-M	5389	3.92E+12	12585	1.16E+12	11897
	0211011T-M	1095	4.12E+13	943	3.92E+13	

name	4.2 K				
	sample number	density (cm ⁻²)	SdH density (cm ⁻²)	PL (eV)	ISBA (eV)
A	0111121T-M	1.74E+12	1.07E+12		2.11E-01
	0111122T-M				
	0112201T-M				
	0112202T-M				
B	0201181T-M	-	9.07E+11	5.16E-01	2.74E-01
C	0201182T-M	1.54E+13	6.11E+11	5.00E-01	2.44E-01
W	0201251T-M	-		6.28E-01	3.27E-01
	0201252T-M			5.78E-01	
	0203062T-M				
D	0205171T-M	9.17E+13	3.47E+12		2.48E-01
	0205201T-M				
E	0205221T-M			4.93E-01	
	0205241T-M			3.74E-01	
	0205271T-M			3.85E-01	
	0205291T-W			5.67E-01	
	0206031T-W				
	0206051T-M			5.94E-01	
	0206071T-M			5.31E-01	
	0207102T-W			5.00E-01	
	0207152T-W				
	0207221T-W				
	0207222T-M				
	0207241T-W			5.01E-01	
	0207242T-M			split	
	0207291T-W			5.13E-01	
	0207292T-M			split	
	0207311T-W			split	
	0207312T-M				
	0208021T-W			3.23E-01	
	0208022T-M				
	0208061T-W			3.79E-01	
	0208081T-W				
	0208211T-W			5.97E-01	
	0208212T-M				
	0208271T-W				
	0208272T-M				
	0208291T-W				
	0208292T-M				
	0209021T-W				
	0209022T-M	-			2.87E-01
	0209041T-W				
F	0209042T-M	1.21E+12	9.67E+11		2.02E-01
	0209091T-M				x
G	0209111T-M	9.46E+11	3.08E+11		1.97E-01
	0211011T-M				

name	other information
A	
B	
C	RICE: SdH=6E11
W	
D	RICE: SdH=3.44E12
E	RICE: SdH=2.02E12
F	
G	70nm AlSb layer on InAs layer

name	period	sample number	sub.	InAs thickness	QW period	interface2 (on InAs)	interface1 (on AlSb)	doping
H	7	0211012T-M	GaAs	10.0	20	InSb(3.6s)	InSb(3.6s)	
I	9	0211062T-M	GaAs	10.0	20	AlAs(3.6s)	InSb(3.6s)	
	10	0211081T-W	GaSb	7.0	20	InSb(3.6s)	InSb(3.6s)	
J	11	0211082T-M	GaAs	7.0	20	InSb(3.6s)	InSb(3.6s)	
	12	0211111T-W	GaSb	7.5	20	InSb(3.6s)	InSb(3.6s)	
	13	0211112T-M	GaAs	7.5	20	InSb(3.6s)	InSb(3.6s)	
K	14	0211131T-M	GaAs	6.5	20	InSb(3.6s)	InSb(3.6s)	
L	16	0211151T-M	GaAs	6.0	20	InSb(3.6s)	InSb(3.6s)	
M	19	0211182T-M	GaAs	5.0	20	InSb(3.6s)	InSb(3.6s)	
	20	0211201T-M	GaAs	4.5	20	InSb(3.6s)	InSb(3.6s)	
	22	0211221T-M	GaAs	8.0	20	InSb(3.6s)	InSb(3.6s)	
	24	0211291T-W	GaSb	3.3	20	InSb(3.6s)	InSb(3.6s)	
	25	0211292T-W	GaSb	3.3	20	InSb(3.6s)	InSb(3.6s)	
N	28	0212062T-M	GaAs	10.0	1	InSb(3.6s)	InSb(3.6s)	
O	29	0212091T-W	GaAs	dqw	20	InSb(3.6s)	InSb(3.6s)	
P	31	0212111T-W	GaAs	dqw	20	InSb(3.6s)	InSb(3.6s)	
	36	0212162T-W	GaAs	7.3	20	InSb(3.6s)	InSb(3.6s)	
	4	0302071T-W	GaAs	4.0	20	InSb(3.6s)	InSb(3.6s)	
	6	0302121T-W	GaAs	dqw	10	InSb(3.6s)	InSb(3.6s)	
	7	0302122T-W	GaAs	dqw	10	InSb(3.6s)	InSb(3.6s)	
	13	0302261T-W	GaAs	4.0	20	InSb(3.6s)	InSb(3.6s)	
	15	0302281T-W	GaAs	3.0	20	InSb(3.6s)	InSb(3.6s)	
	17	0303051T-W	GaAs	10.0	20	InSb(3.6s)	InSb(3.6s)	
	21	0303171T-W	GaAs	10.0	10	InSb(3.6s)	InSb(3.6s)	
	22	0303172T-W	GaAs	10.0	10	InSb(3.6s)	InSb(3.6s)	
Q	9	0306112T-W	GaAs	10.0	20	InSb(3.6s)	InSb(3.6s)	
R	10	0306131T-W	GaAs	5.0	20	InSb(3.6s)	InSb(3.6s)	Si
	11	0306132T-W	GaAs	3.0	20	InSb(3.6s)	InSb(3.6s)	Si
S	14	0306181T-W	GaAs	4.0	20	InSb(3.6s)	InSb(3.6s)	Si
T	16	0306201T-W	GaAs	3.0	20	InSb(3.6s)	InSb(3.6s)	Si
	18	0306231T-W	GaAs	3.0	20	InSb(3.6s)	InSb(3.6s)	
U	22	0306271T-W	GaAs	dqw	10	InSb(3.6s)	InSb(3.6s)	Si
V	23	0306272T-W	GaAs	dqw	10	InSb(3.6s)	InSb(3.6s)	
	30	0307071T-W	GaAs	2.0	20	InSb(3.6s)	InSb(3.6s)	Si
	32	0307091T-W	GaAs	2.0	20	InSb(3.6s)	InSb(3.6s)	Si
	34	0307141T-W	GaAs	1.5	20	InSb(3.6s)	InSb(3.6s)	Si

name	sample number	300K Hall		77K Hall		4.2 K Hall
		mobility (cm ² /Vs)	density (cm ⁻²)	mobility (cm ² /Vs)	density (cm ⁻²)	mobility (cm ² /Vs)
H	0211012T-M	11849	6.67E+13	20907	6.59E+13	24343
I	0211062T-M	7856	6.98E+13	13600	6.85E+13	-
	0211081T-W					
J	0211082T-M	5679	2.63E+13	8259	2.46E+13	-
	0211111T-W					
	0211112T-M	6404	2.49E+13	9714	2.30E+13	-
K	0211131T-M	5414	1.94E+13	7477	1.75E+13	
L	0211151T-M	4683	1.62E+13	5355	1.58E+13	
M	0211182T-M	2917	1.61E+13	3290	1.36E+13	-
	0211201T-M	2314	1.22E+13	2135	9.69E+12	
	0211221T-M	5925	1.15E+13	9899	8.86E+12	
	0211291T-W					
	0211292T-W					
N	0212062T-M	11054	2.86E+12	30578	1.97E+12	33545
O	0212091T-W	3376	1.34E+13	4207	9.27E+12	-
P	0212111T-W	3876	9.12E+12	6007	5.20E+12	
	0212162T-W	3362	6.79E+12	3572	4.51E+12	
	0302071T-W	109	2.79E+14	42	4.56E+14	
	0302121T-W	3184	7.62E+12	10526	2.73E+12	
	0302122T-W	3858	5.75E+12	13002	2.07E+12	
	0302261T-W	354	3.23E+13	896	1.12E+13	
	0302281T-W	100	1.14E+14	406	1.50E+13	
	0303051T-W	4977	4.38E+12	2405	3.37E+12	
	0303171T-W	5579	3.27E+12	4215	1.82E+12	
	0303172T-W	12175	2.57E+12	83004	1.16E+12	
Q	0306112T-W	11552	2.42E+13	19144	2.37E+13	
R	0306131T-W	3790	4.25E+13	4116	4.30E+13	
	0306132T-W	1387	3.79E+13	1171	3.81E+13	
S	0306181T-W	2313	6.10E+13	2317	6.21E+13	
T	0306201T-W	1271	5.81E+13	1148	5.91E+13	
	0306231T-W	3457	9.21E+12	5086	4.98E+12	
U	0306271T-W	10616	2.38E+13	17129	2.23E+13	
V	0306272T-W	16603	1.42E+13	43244	1.42E+13	
	0307071T-W	490	7.05E+13	389	6.83E+13	
	0307091T-W	480	1.02E+14	395	1.01E+14	
	0307141T-W	916	3.28E+13	271	8.69E+13	

name	sample number	density (cm ⁻²)	4.2 K		
			SdH density (cm ⁻²)	PL (eV)	ISBA (eV)
H	0211012T-M	6.75E+13	2.39E+12		2.03E-01
I	0211062T-M	-	1.84E+12		2.14E-01
	0211081T-W				
J	0211082T-M	-			2.96E-01
	0211111T-W				
	0211112T-M	-	8.35E+11	4.91E-01	2.76E-01
K	0211131T-M				
L	0211151T-M				
M	0211182T-M	-			3.75E-01
	0211201T-M				
	0211221T-M				
	0211291T-W				
	0211292T-W				
N	0212062T-M	1.69E+12	1.11E+12		2.00E-01
O	0212091T-W	-		5.35E-01	split
P	0212111T-W				
	0212162T-W				
	0302071T-W				
	0302121T-W				
	0302122T-W				
	0302261T-W				
	0302281T-W			4.91E-01	
	0303051T-W				
	0303171T-W				
	0303172T-W				
Q	0306112T-W				
R	0306131T-W				
	0306132T-W				5.32E-01
S	0306181T-W				4.22E-01
T	0306201T-W				5.35E-01
	0306231T-W			5.35E-01	
U	0306271T-W				1.26E-01
V	0306272T-W				split
	0307071T-W				
	0307091T-W				
	0307141T-W				

name	other information
H	RICE: SdH=2.5E12
I	
J	
K	
L	
M	
N	
O	AlSb(10nm)/InAs(6.058nm)/AlSb(1.227nm)/InAs(6.058nm)/AlSb(10nm)
P	AlSb(10nm)/InAs(6.058nm)/AlSb(1.534nm)/InAs(6.058nm)/AlSb(10nm)
	AlSb(10nm)/InAs(6.058nm)/AlSb(0.92nm)/InAs(6.058nm)/AlSb(10nm)
	AlSb(10nm)/InAs(6.058nm)/AlSb(0.6135nm)/InAs(6.058nm)/AlSb(10nm)
	10nm InAs cap
	10 nm InAs cap
Q	5nm InAs cap
R	5nm InAs cap
	5nm InAs cap
S	5nm InAs cap
T	5nm InAs cap
U	AlSb(10nm)/InAs(14.237nm)/AlSb(0.92nm)/InAs(5.755nm)/AlSb(10nm)
V	AlSb(10nm)/InAs(14.237nm)/AlSb(0.92nm)/InAs(5.755nm)/AlSb(11nm)
	5nm InAs cap
	5nm InAs cap
	5nm InAs cap

8 References

-
- ¹ E. R. Mueller, "Terahertz Radiation: Applications and Sources," *The Industrial Physicist* Aug./Sept., 27 (2003).
- ² J. M. Chamberlain, R. E. Miles, C. E. Collins, and D. P. Steenson, "Introduction to Terahertz Solid-State Devices," in *New Directions in Terahertz Technology*, eds. J. M. Chamberlain and R. E. Miles, Kluwer, the Netherlands, 1997.
- ³ H. H. Weits and D. Oepts, "Continuously tunable, high-power, single-mode radiation from a short-pulse free-electron laser," *Phys. Rev. E* **60**, 946 (1999).
- ⁴ F. Keilmann, V. N. Shastin, and R. Till, "Pulse buildup of the germanium far-infrared laser," *Appl. Phys. Lett.* **58**, 2205 (1991).
- ⁵ D. H. Auston, "Ultrafast Optoelectronics," in: *Ultrashort Laser Pulses: Generation and Applications, 2nd Edition*, edited by W. Kaiser (Springer-Verlag, Berlin, 1993), pp. 183-234; D. H. Auston, "Picosecond optoelectronic switching and gating in silicon," *Appl. Phys. Lett.* **26**, 101 (1975); D. H. Auston, "Picosecond photoconducting Hertzian dipoles," *Appl. Phys. Lett.* **45**, 284 (1984); C. Fattinger and D. Grischkowsky, "Point source terahertz optics," *Appl. Phys. Lett.* **53**, 1480 (1988); C. Fattinger and D. Grischkowsky, "Terahertz beams," *Appl. Phys. Lett.* **54**, 490 (1989).
- ⁶ S. L. Chuang, S. Schmitt-Rink, B. I. Greene, P. N. Saeta, and A. F. J. Levi, "Optical rectification at semiconductor surfaces," *Phys. Rev. Lett.* **68**, 102 (1992).

-
- ⁷ Y. S. Lee, T. Meade, T. B. Norris, and A. Galvanauskas, "Tunable narrow-band terahertz generation from periodically poled lithium niobate," *Appl. Phys. Lett.* **78**, 3583 (2001).
- ⁸ C. Weiss, G. Torosyan, Y. Avetisyan, and R. Beigang, "Generation of tunable narrow-band surface-emitted terahertz radiation in periodically poled lithium niobate," *Optics Lett.* **26**, 563 (2001).
- ⁹ E. R. Brown, K. A. McIntosh, K. B. Nichols, and C. L. Dennis, "Photomixing up to 3.8 THz in low-temperature-grown GaAs," *Appl. Phys. Lett.* **66**, 285 (1995).
- ¹⁰ K. Kawase, J. Shikata, and H. Ito, "Narrow-linewidth tunable terahertz-wave sources using nonlinear optics," *Topics in Applied Physics* **89**, 397 (2003).
- ¹¹ F. Capasso, D. L. Sivco, C. Sirtori, A. L. Hutchinson, and A. Y. Cho, "Quantum Cascade Laser," *Science* **264**, 553 (1994).
- ¹² R. Kohler, A. Tredicucci, F. Beltram, H. E. Beere, E. H. Linfield, A. G. Davies, D. A. Ritchie, "Low-threshold quantum-cascade lasers at 3.5 THz ($\lambda = 85 \mu\text{m}$)," *Optics Lett.* **28**, 810 (2003).
- ¹³ B. S. Williams, S. Kumar, H. Callebaut, Q. Hu, and J. L. Reno, "Terahertz quantum-cascade laser at $\lambda \sim 100 \mu\text{m}$ using metal waveguide for mode confinement," *Appl. Phys. Lett.* **83**, 2124 (2003).
- ¹⁴ M. Rochat, L. Ajili, H. Willenberg, J. Faist, H. Beere, G. Davies, E. Linfield, and D. Ritchie, "Low-threshold terahertz quantum-cascade lasers," *Appl. Phys. Lett.* **81**, 1381 (2002).
- ¹⁵ O. Gauthier-Lafaye, P. Boucaud, F. H. Julien, S. Sauvage, S. Cabaret, J.-M. Lourtioz, V. Thierry-Mieg and R. Planel, "Long-wavelength (15.5 μm) unipolar semiconductor laser in GaAs quantum wells," *Appl. Phys. Lett.* **71**, 3691 (1997).

-
- ¹⁶ C. Sirtori, F. Capasso, J. Faist, L. N. Pfeiffer, and K. W. West, “Far-infrared generation by doubly resonant difference frequency mixing in a coupled quantum well two-dimensional electron gas system,” *Appl. Phys. Lett.* **65**, 445 (1994).
- ¹⁷ I. Vurgaftman, J. R. Meyer, and L. R. Ram-Mohan, “Band parameters for III-V compound semiconductors and their alloys,” *J. Appl. Phys.* **89**, 5815 (2001).
- ¹⁸ Ansheng Liu and C. Z. Ning, “Near-infrared laser pumped intersubband THz laser gain in InGaAs–AlAsSb–InP quantum wells,” *Appl. Phys. Lett.* **76**, 1984 (2000).
- ¹⁹ M. Yano, M. Okuizumi, Y. Iwai, and M. Inoue, “Molecular-beam-epitaxial growth and optical analysis of InAs/AlSb strained-layer superlattices,” *J. Appl. Phys.* **74**, 7472 (1993).
- ²⁰ K. Ohtani and H. Ohno, “InAs/AlSb quantum cascade lasers operating at 10 μm ,” *Appl. Phys. Lett.* **82**, 1003 (2003).
- ²¹ G. Tuttle, H. Kroemer, and J. H. English, “Effects of interface layer sequencing on the transport properties of InAs/AlSb quantum wells: Evidence for antisite donors at the InAs/AlSb interface,” *J. Appl. Phys.* **67**, 3032 (1990).
- ²² S. Datta, *Electronic Transport in Mesoscopic Systems*, Cambridge U. Press, New York, 1995.
- ²³ P. Y. Yu and M. Cardona, *Fundamentals of Semiconductors*, 3rd ed., sec. 5.5.3, Springer-Verlag, New York, 2001.
- ²⁴ Y. Sato, T. Kita, S. Gozu, and S. Yamada, “Large spontaneous spin splitting in gate-controlled two-dimensional electron gasses at normal In_{0.75}Ga_{0.25}As/In_{0.75}Al_{0.25}As heterojunctions,” *J. Appl. Phys.* **89**, 8017 (2001).

-
- ²⁵ H. Kroemer, C. Nguyen, and B. Brar, “Are there Tamm-state donors at the InAs-AlSb quantum well interface?”, *J. Vac. Sci. Technol. B* **10**, 1769 (1992).
- ²⁶ S. Ideshita, A. Furukawa, Y. Mochizuki, and M. Mizuta, *Appl. Phys. Lett.* **60**, 2549 (1992).
- ²⁷ G. Tuttle, H. Kroemer, and J. H. English, “Effects of interface layer sequencing on the transport properties of InAs/AlSb quantum wells: Evidence for antisite donors at the InAs/AlSb interface,” *J. Appl. Phys.* **67**, 3032 (1990).
- ²⁸ C. Nguyen, B. Brar, H. Kroemer, and J. H. English, “Surface donor contribution to electron sheet concentrations in not-intentionally doped InAs-AlSb quantum wells,” *Appl. Phys. Lett.* **60**, 1854 (1992).
- ²⁹ C. Nguyen, B. Brar, and H. Kroemer, “Surface-layer modulation of electron concentrations in InAs-AlSb quantum wells,” *J. Vac. Sci. Tech. B* **11**, 1706 (1993).
- ³⁰ G. Dresselhaus, A. F. Kip, and C. Kittel, “Observation of Cyclotron Resonance in Germanium Crystals,” *Phys. Rev.* **92**, 827 (1953).
- ³¹ S. J. Allen, Jr., D. C. Tsui, and J. V. Dalton, “Far-Infrared Cyclotron Resonance in the Inversion Layer of Silicon,” *Phys. Rev. Lett.* **32**, 107 (1974).
- ³² J. Kono, “Cyclotron Resonance,” in: *Methods in Materials Research*, eds. E. N. Kaufmann, R. Abbaschian, A. Bocarsly, C.-L. Chien, D. Dollimore, B. Doyle, A. Goldman, R. Gronsky, S. Pearton, and J. Sanchez, Unit 9b.2, Wiley, New York, 2001.
- ³³ D. C. Larrabee, G. A. Khodaparast, F. K. Tittel, J. Kono, M. Rochat, L. Ajili, J. Faist, H. Beere, E. Linfield, Y. Nakajima, M. Nakai, S. Sasa, M. Inoue, S. J. Chung, and M. B. Santos,

“Application of Terahertz Quantum Cascade Lasers to Semiconductor Cyclotron Resonance,”
Optics Letters, in press.

³⁴ M. Rochat, L. Ajili, H. Willenberg, J. Faist, H. Beere, G. Davies, E. Linfield, and D. Ritchie,
“Low-threshold terahertz quantum-cascade lasers,” *Appl. Phys. Lett.* **81**, 1381 (2002).

³⁵ A. Barkan and D. Mittleman (daniel@rice.edu), private communication.

³⁶ R. A. Stradling and R. A. Wood, “The temperature dependence of the band-edge effective
masses of InSb, InAs and GaAs as deduced from magnetophonon magnetoresistance
measurements,” *J. Phys. C* **3**, L94 (1970).

³⁷ C. R. Pidgeon and R. N. Brown, “Interband magneto-absorption and Faraday rotation in InSb,”
Phys. Rev. **146**, 575 (1966).

³⁸ J. Tang, “Fourier Transform Infrared Spectroscopy of 6.1-Angstrom Semiconductor Quantum
Wells,” M. S. thesis, Rice University, 2002.

³⁹ R. J. Warburton, K. Weilhammer, J. P. Kotthaus, M. Thomas, and H. Kroemer, “Influence of
Collective Effects on the Linewidth of Intersubband Resonance,” *Phys. Rev. Lett.* **80**, 2185
(1998).

⁴⁰ R. J. Warburton, C. Gauer, A. Wixforth, J. P. Kotthaus, B. Brar, and H. Kroemer,
“Intersubband resonances in InAs/AlSb quantum wells: Selection rules, matrix elements, and the
depolarization field,” *Phys. Rev. B* **53**, 7903 (1996).

⁴¹ B. F. Levine, S. D. Gunapala, J. M. Kuo, S. S. Pei, and S. Hui, “Normal incidence hole
intersubband absorption long wavelength GaAs/Al_xGa_{1-x}As quantum well infrared
photodetectors,” *Appl. Phys. Lett.* **59**, 1864 (1991).

-
- ⁴² H. C. Liu, B. F. Levine, and J. Y. Andersson, *Quantum Well Intersubband Transition Physics and Devices*, Kluwer Academic Publishers, Boston, 1994.
- ⁴³ I. Prevot, B. Vinter, F. H. Julien, F. Fossard, and X. Marcadet, “Experimental and theoretical investigation of interband and intersubband transitions in type-II InAs/AlSb superlattices,” *Phys. Rev. B* **64**, 195318 (2001).
- ⁴⁴ B. C. Covington, C. C. Lee, B. H. Hu, H. F. Taylor, and D. C. Streit, “Infrared intersubband absorption in GaAs/AlAs multiple quantum wells,” *Appl. Phys. Lett.* **54**, 2145 (1989).
- ⁴⁵ M. O. Manasreh, F. Szmulowicz, D. W. Fischer, K. R. Evans, and C. E. Stutz, “Intersubband infrared absorption in a GaAs/Al_{0.3}Ga_{0.7}As quantum well structure,” *Appl. Phys. Lett.* **57**, 1790 (1990).
- ⁴⁶ E. B. Dupont, D. Delacourt, D. Papillon, J. P. Schnell, and M. Papuchon, “Influence of ionized impurities on the linewidth of intersubband transitions in GaAs/GaAlAs quantum wells,” *Appl. Phys. Lett.* **60**, 2121 (1992).
- ⁴⁷ J. Li, K. I. Kolokolov, C. Z. Ning, D. C. Larrabee, G. A. Khodaparast, J. Kono, K. Ueda, Y. Nakajima, S. Sasa, and M. Inoue, “Intersubband Transitions in InAs/AlSb Quantum Wells,” *MRS Proceedings Volume 744, Progress in Semiconductors II – Electronics and Optoelectronic Applications*, ed. B. D. Weaver, M. O. Manasreh, C. C. Jagadish, and S. Zollner (Materials Research Society, 2003), pp. M9.2.1-M9.2.12.
- ⁴⁸ E. B. Dupont, D. Delacourt, D. Pappilon, J. P. Schnell, and M. Papuchon, “Influence of ionized impurities on the linewidth of intersubband transitions in GaAs/GaAlAs quantum wells,” *Appl. Phys. Lett.* **60**, 2121 (1992).

-
- ⁴⁹ K. L. Campman, H. Schmidt, A. Imamoglu, and A. C. Gossard, "Interface roughness and alloy-disorder scattering contributions to intersubband transition linewidths," *Appl. Phys. Lett.* **69**, 2554 (1996).
- ⁵⁰ K. Ohtani, N. Matsumoto, H. Sakuma, and H. Ohno, "Intersubband absorption in *n*-doped InAs/AlSb multiple-quantum-well structures," *Appl. Phys. Lett.* **82**, 37 (2003).
- ⁵¹ I. Prevot, B. Vinter, F. H. Julien, F. Fossard, and X. Marcadet, "Experimental and theoretical investigation of interband and intersubband transitions in type-II InAs/AlSb superlattices," *Phys. Rev. B* **64**, 195318 (2001).
- ⁵² P. Ramvall, B. Kowalski, and P. Omling, "Zero-magnetic-field spin splittings in $\text{Al}_x\text{Ga}_{1-x}\text{As}/\text{GaAs}$ heterojunctions," *Phys. Rev. B* **55**, 7160 (1997).
- ⁵³ J. Luo, H. Munekata, F. F. Fang, and P. J. Stiles, "Observation of the zero-field spin splitting of the ground electron subband in GaSb-InAs-GaSb quantum wells," *Phys. Rev. B* **38**, 10142 (1988).
- ⁵⁴ D. Grundler, "Large Rashba Splitting in InAs Quantum Wells due to Electron Wave Function Penetration into the Barrier Layers," *Phys. Rev. Lett.* **84**, 6074 (2000).
- ⁵⁵ J. P. Heida, B. J. van Wees, J. J. Kuipers, T. M. Klapwijk, and G. Borghs, "Spin-orbit interaction in a two-dimensional electron gas in a InAs/AlSb quantum well with gate-controlled electron density," *Phys. Rev. B* **57**, 11911 (1998).
- ⁵⁶ J. T. Olesberg, W. H. Lau, M. E. Flatté, C. Yu, E. Altaunkaya, E. M. Shaw, T. C. Hasenberg, and T. F. Boggess, "Interface contributions to spin relaxation in a short-period InAs/GaSb superlattice," *Phys. Rev. B* **64**, 201301 (2001).

-
- ⁵⁷ A. D. Wieck, E. Batke, D. Heitmann, J. P. Kotthaus, and E. Bangert, "Lifting of the Spin Degeneracy of Hole Subbands in a Surface Electric Field on Silicon," *Phys. Rev. Lett.* **53**, 493 (1984).
- ⁵⁸ G. Bastard, *Wave Mechanics Applied to Semiconductor Heterostructures*, Les Editions de Physique, Les Ulis, France and Wiley, NY, 1988.
- ⁵⁹ P. Y. Yu and M. Cardona, *Fundamentals of Semiconductors: Physics and Materials Properties*, 3rd edition, Springer-Verlag, New York, 2001.
- ⁶⁰ W. A. Harrison, *Solid State Theory*, Dover, New York, 1980.
- ⁶¹ C. Hermann and C. Weisbuch, "Optical Detection of Conduction-Electron Spin-Resonance in GaAs, Ga_{1-x}In_xAs, and Ga_{1-x}Al_xAs," *Phys. Rev. B* **15**, 816 (1977).
- ⁶² J. Li, K. I. Kolokolov, C. Z. Ning, D. C. Larrabee, G. A. Khodaparast, J. Kono, K. Ueda, Y. Nakajima, S. Sasa, and M. Inoue, "Microscopic Modeling of Intersubband Resonances in InAs/AlSb Quantum Wells," *Physica E*, in press.
- ⁶³ H. Haug and S. W. Koch, *Quantum Theory of the Optical and Electronic Properties of Semiconductors*, 3rd edition, World Scientific, River Edge, NJ, 1994.
- ⁶⁴ D. E. Nikonov, A. Imamoğlu, L. V. Butov, and H. Schmidt, "Collective Intersubband Excitations in Quantum Wells: Coulomb Interaction versus Subband Dispersion," *Phys. Rev. Lett.* **79**, 4633 (1997).
- ⁶⁵ N. W. Ashcroft and N. D. Mermin, *Solid State Physics*, ch. 17, Harcourt Brace, Orlando, 1976.
- ⁶⁶ S. J. Allen, D. C. Tsui, and B. Vinter, "On the absorption of infrared radiation by electrons in semiconductor inversion layers," *Solid State Commun.* **20**, 425 (1976).

⁶⁷ T. Ando, "Inter-Subband Optical-Transitions in a Surface Space-Charge Layer," *Solid State Commun.* **21**, 133 (1977).